

ISSN: (Print) (Online) Journal homepage: <https://www.tandfonline.com/loi/tbsd20>

Genetic complementation screening and molecular docking give new insight on phosphorylation-dependent Mastl kinase activation

Mehmet Erguven, Seval Kilic, Ezgi Karaca & M. Kasim Diril

To cite this article: Mehmet Erguven, Seval Kilic, Ezgi Karaca & M. Kasim Diril (2022): Genetic complementation screening and molecular docking give new insight on phosphorylation-dependent Mastl kinase activation, Journal of Biomolecular Structure and Dynamics, DOI: [10.1080/07391102.2022.2131627](https://doi.org/10.1080/07391102.2022.2131627)

To link to this article: <https://doi.org/10.1080/07391102.2022.2131627>



View supplementary material [↗](#)



Published online: 21 Oct 2022.



Submit your article to this journal [↗](#)







View related articles [↗](#)



View Crossmark data [↗](#)

Genetic complementation screening and molecular docking give new insight on phosphorylation-dependent Mastl kinase activation

Mehmet Erguven^{a,b} , Seval Kilic^{a,b} , Ezgi Karaca^{a,b}  and M. Kasim Diril^{a,b,c} 

^aIzmir Biomedicine and Genome Center, Izmir, Turkey; ^bIzmir International Biomedicine and Genome Institute, Dokuz Eylul University, Izmir, Turkey; ^cDepartment of Medical Biology, Faculty of Medicine, Dokuz Eylul University, Izmir, Turkey

Communicated by Ramaswamy H. Sarma

ABSTRACT

Mastl is a mitotic kinase that is essential for error-free chromosome segregation. It is an atypical member of AGC kinase family, possessing a unique non-conserved middle region. The mechanism of Mastl activation has been studied extensively *in vitro*. Phosphorylation of several residues were identified to be crucial for activation. These sites correspond to T193 and T206 in the activation loop and S861 in the C-terminal tail of mouse Mastl. To date, the significance of these phosphosites was not confirmed in intact mammalian cells. Here, we utilize a genetic complementation approach to determine the essentials of mammalian Mastl kinase activation. We used tamoxifen-inducible conditional knockout mouse embryonic fibroblasts to delete endogenous Mastl and screened various mutants for their ability to complement its loss. S861A mutant was able to complement endogenous Mastl loss. In parallel, we performed computational molecular docking studies to evaluate the significance of this residue for kinase activation. Our in-depth sequence and structure analysis revealed that Mastl pS861 does not belong to a conformational state, where the phosphoresidue contributes to C-tail docking. C-tail of Mastl is relatively short and it lacks a hydrophobic (HF) motif that would otherwise help its anchoring over N-lobe, required for the final steps of kinase activation. Our results show that phosphorylation of Mastl C-tail turn motif (S861) is dispensable for kinase function *in cellulo*.

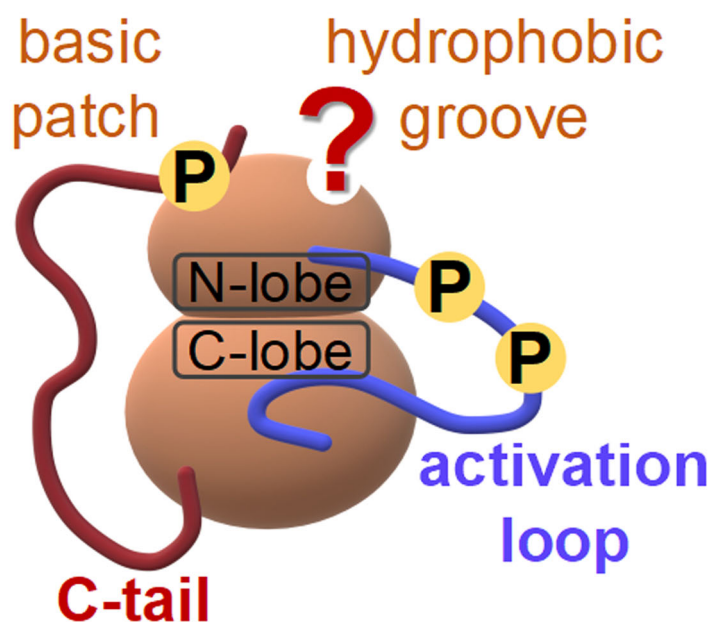
ARTICLE HISTORY

Received 26 August 2022
Accepted 26 September 2022

KEYWORDS

Mastl; kinase activation; phosphorylation; cell cycle; HADDOCK

Mastl kinase



Abbreviations: 4-OHT: 4-hydroxytamoxifen; CKO: conditional knockout; CSF: cytostatic factor; DMSO: dimethyl sulfoxide; HA: human influenza hemagglutinin; HF: hydrophobic motif; MBP: myelin basic

protein; MEF: mouse embryonic fibroblast; NCMR: non-conserved middle region; NLT: N-lobe tether; PDB: the protein data bank; SAC: spindle assembly checkpoint; WT: wild-type; KD: kinase-dead

1. Introduction

1.1. Function of *Mastl* in mitosis

Post-translational regulation by phosphorylation is the major regulator of mitosis. Initiation of mitosis is governed by mitotic protein kinases (Kim et al., 2016). Cdk1 is present at the top of the mitotic signaling cascade (Diril et al., 2012; Santamaría et al., 2007). Cdk1 and its downstream protein kinases activate their mitotic substrates, initiating a signaling cascade. Most of these phosphorylations result in activation of factors that promote mitosis and inhibition of factors that promote mitotic exit (Gharbi-Ayachi et al., 2010). PP2A (protein phosphatase 2A) is the primary antagonist of Cdk1 during mitosis. This phosphatase is indirectly inhibited by *Mastl* (Microtubule-associated serine/threonine kinase like). *Mastl* is the human orthologue of Greatwall kinase (Gwl), first identified in *Drosophila* (Yu et al., 2004). *Mastl* kinase phosphorylates two highly homologous, small, thermostable proteins: Arpp19 and ENSA. These two phosphoproteins specifically bind and inhibit B55 δ -bound PP2A. Inhibition of PP2A-B55 δ results in rapid accumulation of phosphorylations on mitotic substrates, supporting the autoamplification loop (Kim et al., 2012; Kishimoto, 2015; Mochida & Hunt, 2012; Mochida et al., 2010; Slupe et al., 2011).

Due to this crucial function in mitosis, *Mastl* is an essential protein kinase for cell division and proliferation. Loss-of-function studies have shown that, in its absence, SAC (Spindle Assembly Checkpoint) signaling is weakened, resulting in premature onset of anaphase. Spindle-kinetochore attachment errors cannot be corrected, leading to anaphase bridges and DNA breaks during chromosome segregation (Bisteau et al., 2020; Diril et al., 2016). Anaphase bridges prevent closure of the cleavage furrow, causing mitotic collapse at the end of mitosis (Alvarez-Fernandez et al., 2013).

1.2. Activation mechanism of AGC family protein kinases

The common kinase fold is constituted of a β -sheet-rich smaller N-lobe and an α -helix-rich larger C-lobe, connected through a loop segment. This loop encompasses a 20–30 residue-long activation loop that contains the catalytic aspartate within its conserved DFG (Asp-Phe-Gly) motif (Modi & Dunbrack, 2019). The hinge region, glycine-rich loop's backbone, chelated cofactors and a conserved lysine together coordinate ATP through electrostatic interactions (Endicott et al., 2012) (Figure 1(A)).

According to the general kinase activation model, the active DFG-in conformation is induced by activation loop phosphorylation (Adams, 2003; Vijayan et al., 2015). In its active state, activation loop allows the binding of ATP and peptide substrate to their respective docking sites. Simultaneously, catalytic aspartate approaches these binding sites (Supporting Information Figure S1) (Huse & Kuriyan,

2002; Zhou et al., 2010). In AGC family of protein kinases, phosphorylation of activation loop can only partially activate the enzyme. A unique feature of AGC kinases is that the core catalytic elements need to be stabilized through intramolecular allosteric interactions. A series of conformational changes are induced by C-tail/N-lobe interactions. C-tail has two important regions that directly interact with N-lobe. These are the turn motif and the HF motif (hydrophobic motif, FXXF). According to the currently accepted model, conserved turn motif phosphosite aids docking of C-tail to the basic patch of N-lobe. Extending from this initial docking point, HF motif reaches the hydrophobic groove of N-lobe. HF motif enhances hydrophobic packing by inserting the benzene rings of its conserved phenylalanines into this hydrophobic groove. This hydrophobic packing allows C-tail to reposition the N-lobe α C-helix. Ultimately, the conserved glutamate within α C-helix and the conserved lysine located in ATP binding pocket form a salt bridge. As explained previously at the beginning of this section, this conserved lysine functions in coordination of ATP. In other words, C-tail indirectly aids the active site for coordination of ATP through a multistep intramolecular allosteric regulation (Figure 1(B)). Using the crystal structure of an atypical AGC kinase (Arencibia et al., 2017), human PKC iota (PDB entry 3A8W) (Takimura et al., 2010), the complete molecular machinery is visualized in Supporting Information Figure S2. Of note, PKA possesses a C-tail phosphate that does not contribute to intramolecular interactions (Supporting Information Figure S3), making the generalizability of current model of AGC kinase activation questionable.

1.3. Activation of *Mastl* kinase

Mastl is a unique serine/threonine protein kinase among AGC family kinases. It has an unusually long (~500 residues) linker region between its N-terminal and C-terminal lobes. Studies on *Xenopus* egg extracts have revealed three phosphosites that are critical for activation of *Mastl* (Blake-Hodek et al., 2012; Vigneron et al., 2011). Positions of these residues in mouse *Mastl* are T193, T206 and S861 (T194, T207, S875 in human; T193, T206, S883 in *Xenopus*). T193 and T206 are located in activation loop within Cdk1 consensus motifs (proline-directed) and are phosphorylated by Cdk1 *in vitro*. These two phosphosites are necessary for nuclear export of *Mastl* before NEBD (nuclear envelope breakdown) (Alvarez-Fernandez et al., 2013). Upon phosphorylation, activation loop shifts from DFG-out to DFG-in conformation. Then, *Mastl* undergoes cis-autophosphorylation by phosphorylating its turn motif (tail/linker) phosphosite S861 (Blake-Hodek et al., 2012). As explained in the previous section, in AGC kinases, this turn motif phosphoresidue is docked to a basic patch on N-lobe, serving as a means to guide HF motif towards N-lobe hydrophobic groove. However, in the case of

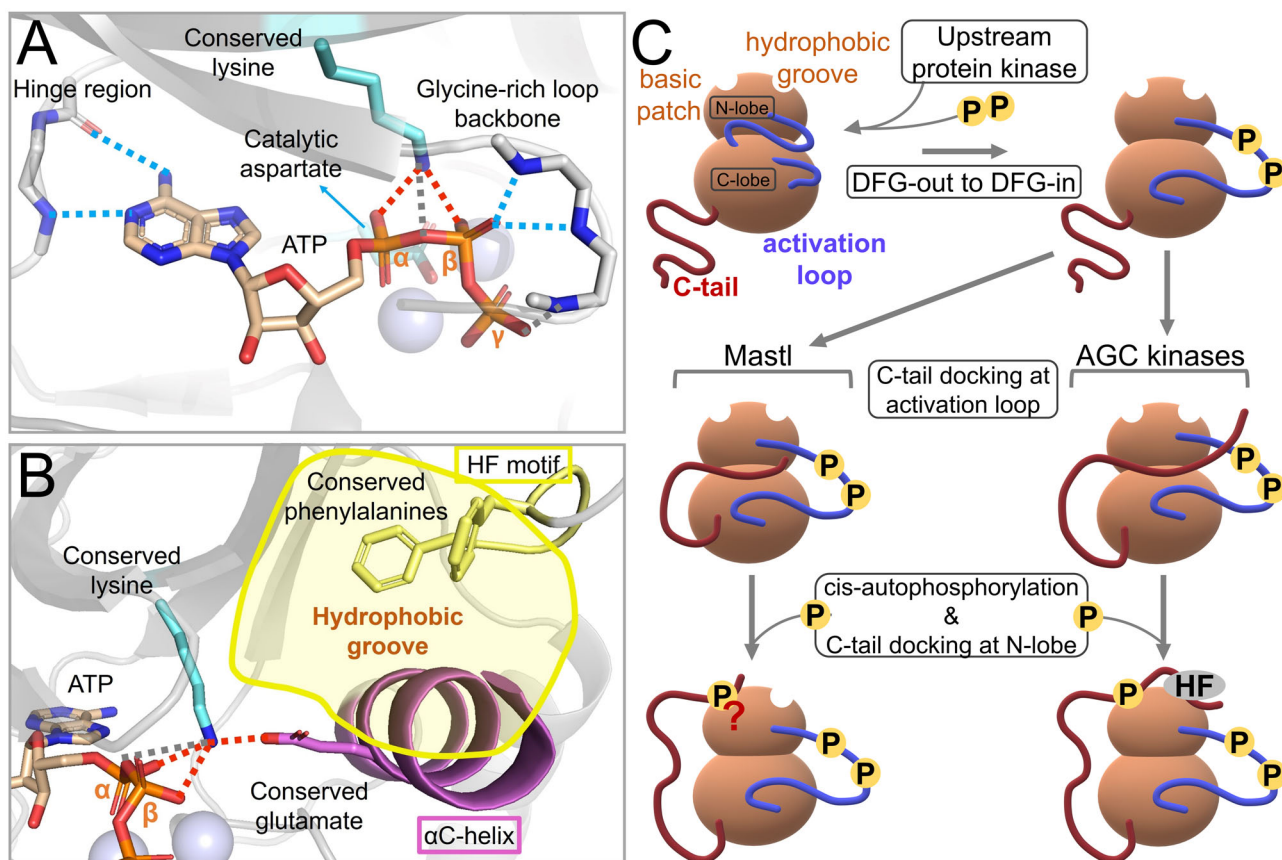


Figure 1. The structural features of AGC kinases. (A) The crystal structure of catalytic subunit of ATP-bound c-AMP-dependent protein kinase (PDB entry 1ATP) (Zheng et al., 1993). The hinge region and glycine-rich loop backbones, catalytic aspartate, conserved lysine and ATP are shown in stick form. The manganese ions are depicted as transparent spheres. The observable ion-ion (salt bridge), ion-dipole and dipole-dipole (hydrogen bonds only) interactions between the enzyme and ATP are depicted as red, gray and blue colored dashed lines, respectively. (B) The crystal structure of catalytic subunit of ATP-bound c-AMP-dependent protein kinase (PDB entry 3X2W) (Das et al., 2015). The conserved lysine and glutamate, conserved phenylalanine residues of HF motif and ATP are shown in stick form. α C-helix (violet), HF motif (yellow) and the proximal β -strand (transparent gray) together form the hydrophobic groove. Hydrophobic groove is indicated by the transparent yellow area. The magnesium ions are depicted as transparent spheres. The observable ion-ion (salt bridge) and ion-dipole interactions between the enzyme and ATP are depicted as red and gray colored dashed lines, respectively. The blue, orange and red colored atoms are nitrogen, phosphorus and oxygen, respectively. (C) Comparison of the general AGC kinase and Mastl kinase activation models. The bilobal protein kinase structure is depicted as light-brown bubbles. The white indents at top-left and top-right positions of N-lobe indicate the basic patch and the hydrophobic groove, respectively. Activation loop and C-tail are depicted as blue and red lines, respectively. The cartoon illustrations show the difference between activation of Mastl (left) and general AGC kinase activation model (right). For simplicity, extended NCMR is not represented in the illustrated Mastl kinase structures.

Mastl, C-tail of the enzyme is shorter and it does not possess a known HF motif. Therefore, it cannot reach the hydrophobic groove (Figure 1(C)).

Results of Vigneron et al. (2011) demonstrated that activity of constitutively active Mastl increases up to 156% in the presence of a synthetic peptide (PIFtide) that mimics hydrophobic motif. Their finding suggests that Mastl utilizes the HF motif of other AGC kinases in a heteromeric complex to complete its activation. However, it is still not clear what purpose would C-tail/N-lobe intramolecular docking would serve, when the C-tail is devoid of HF motif. This raises the question whether the C-tail phosphorylation (S861) is essential for the cellular functions of Mastl.

In the present study, we reevaluated the biological significance of these three phosphosites and two additional phosphosites (S212 and T727) that were proposed to be contributor to Mastl activation (Blake-Hodek et al., 2012; Hermida et al., 2020). Other than these, we tested the hyperactive *Drosophila Scant* mutation K71M (Archambault et al., 2007), thrombocytopenia-associated mutation E166D

(Hurtado et al., 2018), and two different non-conserved middle region (NCMR) deletions (Δ 194–725 and Δ 305–620). We obtained viable Mastl knockout mouse embryonic fibroblasts (MEF) clones that express the ectopic E166D, K71M, S861A or S861D mutants. Given the vital role of turn motif phosphosite S861 in AGC kinase activation, we focused our study on functional characterization of this particular phosphosite.

2. Methods

2.1. Software

CLC Main Workbench 7.9.1 software was used for sequence visualization and analysis (<https://digitalinsights.qiagen.com>). The gel images, immunoblot images and micrographs were processed using Adobe Photoshop and GIMP (version 2.10.12) (The GIMP Development Team, 2019). The plots were drawn in R (v3.6.1) (R Core Team, 2019), invoked by RStudio (v1.2.5001) (RStudio Team, 2015), using the ggplot2 (Kassambara, 2019) R package.

2.2. Structural modeling of Mastl

The crystal structure coordinate files were obtained from the Protein Data Bank (PDB) (<https://www.rcsb.org/>) (Berman et al., 2000). The coordinate files (Supporting Information Table S1) were visualized by using PyMOL (version 2.4.0a0) (Schrödinger LLC, 2015). By the help of the sequence alignments given in one of the reference studies (Blake-Hodek et al., 2012), the domain and motif boundaries of mouse Mastl were determined by using UniProt database (<https://www.uniprot.org/>) (The UniProt Consortium, 2019) and EMBOSS Needle webserver (https://www.ebi.ac.uk/Tools/psa/emboss_needle/) (Rice, 2000). Briefly, the FASTA format sequences were obtained from UniProt and the pairwise sequence alignments were performed using EMBOSS Needle. Based on the determined motif boundaries, the motifs were mapped on the 3D structure visuals for the figures. Mouse Mastl was modeled by MODELLER 9.25 (<https://salilab.org/modeller/>) (Fiser et al., 2000; Martí-Renom et al., 2000; Šali & Blundell, 1993; Webb & Sali, 2016), invoked by MODOMAX (<https://github.com/MehmetErguven/MODOMAX>) (Erguven & Karaca, 2021).

Structural refinements, binding energy and buried surface area calculations were performed using the Guru interface of HADDOCK2.2 web server (<https://milou.science.uu.nl/services/HADDOCK2.2/haddockserver-guru.html>) (van Zundert et al., 2016). When the docking stages are skipped, HADDOCK2.2 is capable of refining the interaction of separate molecules. To refine the C-tail and N-lobe interactions, the protein kinase chain was separated with the N-terminal starting position of C-tail. C-tail and the rest of the protein were submitted as if they were separate chains.

Following changes were applied to the default docking protocol;

- 'Remove non-polar hydrogens?' checkbox was unchecked under the 'Distance restraints' tab.
- 'Define center of mass restraints to enforce contact between the molecules' checkbox was checked under the 'Distance restraints' tab.
- 'Randomize starting orientations', 'Perform initial rigid body minimization' and 'Allow translation in rigid body minimization' checkboxes were unchecked under the 'Advanced sampling parameters' tab.
- 'number of MD steps for rigid body high temperature TAD', 'number of MD steps during first rigid body cooling stage', 'number of MD steps during second cooling stage with flexible side-chains at interface' and 'number of MD steps during third cooling stage with fully flexible interface' parameters were set to 0 under the 'Advanced sampling parameters' tab.

HADDOCK outputs residue-based energy contributions of each interfacial amino acid (expressed in electrostatics, vdW (van der Waals) and electrostatics + vdW energy terms), deposited in *ene-residue.disp* file (located under HADDOCK output folder: structures/it1/water/analysis). For each interface residue, various types of scores were extracted from the HADDOCK runs for its 200 different states. These scores were presented in boxplot format in which the energy distribution

of residues can be compared to one another (Figure 6 and Supporting Information Figure S7). The codes and computational methods used in the present study were adapted from our previous study (<https://github.com/CSB-KaracaLab/BINDKIN>) (Erguven et al., 2021).

Protein surface electrostatics potentials were calculated using the APBS-PDB2PQR software suite web server (<https://server.poissonboltzmann.org/>) (Baker et al., 2001; Dolinsky et al., 2004).

2.3. Molecular cloning

Retroviral expression constructs (pBABE-Puro) for N-terminally HA-tagged mouse Mastl WT, D155N (kinase-dead, KD), E166D (thrombocytopenia-associated mutant) and K71M (Drosophila *Scant* mutation) were generated in Kaldis Laboratory (Institute of Molecular and Cell Biology, Singapore). The other mutations were created by site-directed mutagenesis. The primers used for site-directed mutagenesis are given in Supporting Information Table S2.

2.4. PCR genotyping

A three-primer strategy was utilized for genotyping of Mastl locus, to distinguish FLOX and KO alleles (Figure 2(A)). The primers used for genotyping are given in Supporting Information Table S2. For PCR genotyping, the samples were prepared according to the adapted HotSHOT protocol (Truett et al., 2000). DNA sample of 0.5 μ L and 0.25 units of Taq DNA polymerase (A111103; Ampliqon) was used for each 10 μ L of reaction volume. Final primer concentrations were 1 μ M for 'FOR' and 'REV1' and 0.15 μ M for 'REV2' primers. Thirty-five PCR cycles were performed using 67 °C annealing temperature. Under these optimized conditions, the PCR reaction consistently yields similar intensity bands for Mastl^{FLOX} (300 bp) and Mastl^{KO} (500 bp) alleles from a heterozygous Mastl^{FLOX/KO} cell clone (Figure 2).

2.5. Cell culture, retroviral transduction and stable cell line engineering

PLAT-E cells (Cell Biolabs) and Mastl conditional knockout (CKO) immortalized MEFs (Diril et al., 2016) were grown in DMEM supplemented with 10% FBS and antibiotics. Cells were cultured in a 95% humidified incubator with 5% CO₂ at 37 °C. Lipofectamine 3000 transfection reagent (L3000015; Thermo Scientific) was used for transfection of PLAT-E cells. PLAT-E culture and virus production were carried out according to the manufacturer's instructions. The viral supernatant was harvested on second and third days post-transfection and stored at 4 °C up to a week until use.

Polybrene was mixed with retroviral medium to 8 μ g/mL final concentration, immediately before infection of MEFs. MEFs were transduced at 40% confluence. Viral media collected at the second day of transfection were used in the first round of transduction. One day post-transduction, the used viral media were removed and a second round of transduction was performed by using the viral media that was harvested at the third day of transfection. Eight hours

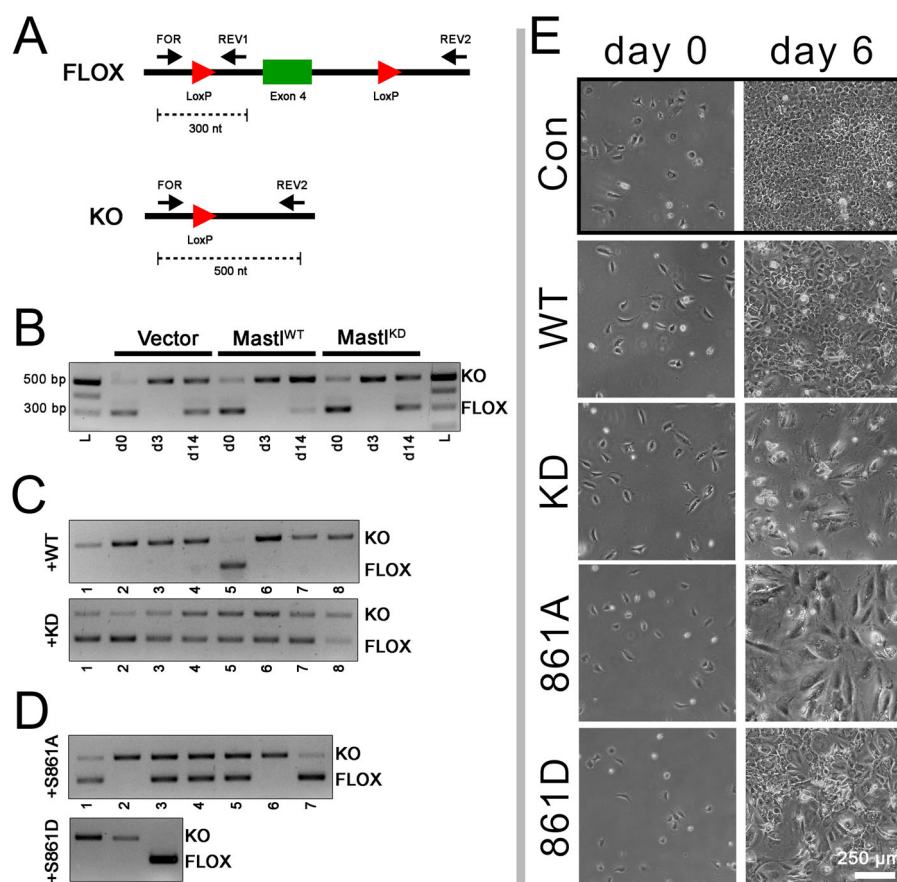


Figure 2. Genotype and phenotype analysis of the ectopic *Mastl*-expressing *Mastl* CKO MEFs. (A) A three-primer strategy was employed for PCR genotyping of the *Mastl* locus. PCR amplification yields 300 and 500 bp fragments for Flox and KO alleles, respectively, at similar intensities from a heterozygous *Mastl*^{Flox/KO} clone's DNA. (B) Stable cell pools were treated with 4-OHT and cells were genotyped at the indicated days. Three days after 4-OHT addition, FLOX allele is undetectable. However, after 14 days, it becomes visible again and especially prominent in stable cell pools infected with empty vector and *Mastl*^{KD} construct. (C) After limited dilution, clonal cell lines were isolated and genotyped. *Mastl*^{WT} construct can complement endogenous *Mastl* loss. Hence, in majority of the clones, endogenous *Mastl* is deleted. None of the *Mastl*^{KD}-infected clones have lost both endogenous *Mastl* loci. (D) From *Mastl*^{861A} and *Mastl*^{861D} infected pools, two homozygous knockout clones could be isolated for both. (E) Proliferation of stable cell pools after deletion of endogenous *Mastl*. The micrographs were acquired immediately before (day 0) and six days (day 6) after 4-OHT treatment. Con indicates uninfected and uninduced parental cells. Scale bar is 250 μ m.

after the second round of transduction, the viral media were removed. Cells were cultured further in normal growth medium overnight for recovery, prior to antibiotic selection. The stable cell lines were generated under 2–4 μ g/mL puromycin selection. Cells were selected for a week and negative control cells died within the first two days of selection. *Mastl* knockout was induced by adding 4-OHT to the culture medium at 20 ng/mL final concentration. The control cells were treated with an equal volume of DMSO. The knockout-induced stable cell lines were subjected to limited dilution approximately 6 days post-induction.

2.6. Western blot and immunocytochemistry

Commercially available primary antibodies used for western blot are rat anti-HA tag (clone 3F10; Roche), rabbit anti-Cyclin B1 (4138S; Cell Signaling Technology), mouse anti-Cdk1 (sc-54; Santa Cruz Biotechnology) and mouse anti-HSP90 (610419; BD Biosciences). The rabbit anti-*Mastl* polyclonal antibody was developed in Kaldis laboratory (Diril et al., 2016).

2.7. Cell viability and proliferation assays

The alamarBlue proliferation assay was carried out in 96-well plate format in three replicates. The daily measurements were initiated one day after seeding the cells. Cells were incubated in 150 μ L of assay medium for 4 h. The assay medium was prepared by diluting 1 volume of alamarBlue dye reagent (BUF012A; Bio-Rad) in 9 volumes of growth medium. The metabolic activity was quantified fluorometrically by using 560 nm excitation wavelength and recording the emission at 590 nm. The assay was performed for six successive days.

The proliferation rate was also measured by a modified 3T3 assay (Diril et al., 2012) in 6-well plates. 20,000 cells were seeded per well and cells were counted after 3 days and 20,000 cells were plated again. Counts were repeated for six successive passages.

3. Results and discussion

3.1. A robust rescue-assay for evaluation of the Mastl mutants

We used the following workflow in order to assess biological significance of the previously described mutations and NCMR deletions (Blake-Hodek et al., 2012; Vigneron et al., 2011). Briefly, (i) CKO Mastl^{FLOX/FLOX} cell pools stably expressing Mastl mutants were generated, (ii) endogenous Mastl gene was deleted by Cre-mediated recombination, (iii) clonal cell lines were isolated and genotyped and (iv) the clones whose endogenous Mastl genes were knocked out were further characterized.

The phosphosites of interest that we screened are T193, T206, S212, T727 and S861. For the phosphosite studies, we have used the T193V, T206V, S212A, T727V, S861A non-phosphorylatable mutants and the T193E, T206E, S861D phosphomimetic mutants. Other Mastl variants in the present study are E166D (thrombocytopenia associated variant) (Hurtado et al., 2018) and K71M (*Scant*) (Archambault et al., 2007) and partial (Δ 305–620) and full (Δ 194–725) NCMR deletions (Blake-Hodek et al., 2012). KD (kinase-dead) variant and WT (wild-type) Mastl were used as negative and positive controls, respectively.

MEFs were infected with retroviral expression constructs (pBABE-Puro) and selected with puromycin, in order to establish stable cell pools expressing ectopic Mastl mutants. To quickly assess complementation capacity of the ectopic constructs, the stable pools were treated with 4-OHT and the cells were collected before and after KO induction (3 and 14 days) were genotyped (Figure 2(A,B)). Due to the nature of the inducible Cre systems, CKO MEFs include a basal level of knockout cells/loci as a result of spontaneous Cre leakage into the nucleus, even without 4-OHT induction (Zhong et al., 2015). Three days post-induction, a complete knockout of Mastl gene was observed. However, within fourteen days, initially undetectable levels of Mastl^{FLOX/FLOX} or Mastl^{FLOX/KO} cells, where endogenous Mastl could not be knocked out, proliferate. Cells escaping knockout is a known disadvantage of the inducible Cre systems (Diril et al. 2012). Cells expressing endogenous Mastl account for majority of the cell population when the ectopic constructs cannot complement endogenous Mastl loss (see day 14 in Figure 2(B)).

Although, nonfunctional Mastl-expressing (i.e., Mastl^{KD}) cell pools eventually proliferate after 4-OHT treatment, there is a lag compared to the functional Mastl-expressing (i.e., Mastl^{WT}) cells. Analysis of different Mastl mutants six days after 4-OHT treatment suggests that S861A, S861D, K71M and E166D mutations retain partial or full kinase activity compared to WT (Figure 2(E) and Supporting Information Figure S5). These results are consistent with the genotyping analysis (Figure 2(C,D) and Supporting Information Figure S4A) which confirms that cells expressing these mutants are viable when their endogenous Mastl is knocked out.

Clonal cell lines were generated after 4-OHT treatment of cell pools expressing various Mastl mutants. PCR genotyping of WT and KD expressing clones confirmed that our experimental system works. When cells had been infected with WT

Mastl, in almost all clones both copies of endogenous Mastl were found to be deleted. Whereas, KD-Mastl-infected clones kept at least one copy of their endogenous Mastl (Figure 2(C)). K71M and E166D Mastl mutants can also complement endogenous Mastl loss (Supporting Information Figures S4 and S5). This is an expected result as these mutations do not have a significant effect on cellular proliferation (Archambault et al., 2007; Hurtado et al., 2018). None of the NCMR deletion clones had homozygous KO genotype, suggesting that the deletions cover catalytic or structural elements that are essential for Mastl function *in vivo*. This is in line with the previous observations for NCMR deletion mutants (Hermida et al., 2020; Vigneron et al., 2011). Conversely, the number of clones we genotyped for our deletion mutants were limited. Therefore, we cannot rule out the fact that with an increased sample size, a homozygous KO clone may be obtained.

After establishing the complementation screening strategy and successfully testing it on known viable mutations (K71M and E166D), we next focused on Mastl phosphorylation sites with putative roles on kinase activation. We created constructs with point mutations that have non-phosphorylatable (T193V, T206V, S212A, T727V and S861A) or phosphomimetic (T193E, T206E and S861D) residues. We were able to isolate clonal cell lines for S861A and S861D, in which, the endogenous Mastl gene was knocked out (Figure 2(D)). Other mutations did not yield viable knockout cell lines in our screen, as all the clones expressed one or both copies of the endogenous Mastl (Supporting Information Figure S4).

3.2. The turn motif phosphosite mutant Mastl is viable

Our complementation screening showed that the turn motif phosphosite mutant-expressing clones (S861A and S861D) were viable when endogenous Mastl gene was deleted. (Figure 2(D)). As previously explained, the turn motif phosphorylation is known to be crucial for AGC kinase activation. Therefore, we focused our study on S861 mutants for functional characterization of this particular phosphosite. We selected one clone from each of the WT, S861A and S861D clonal cell lines for further experiments.

Analysis of the selected clones by immunofluorescence microscopy and western blotting confirmed stable expression of the ectopic constructs (Figure 3). Although the expression levels of the ectopic proteins were lower compared to endogenous Mastl (Figure 3(B)), this was sufficient for cell division. S861A and S861D clones could still proliferate albeit at a slightly reduced rate (Figure 4). The band upshift of the phosphomimetic 861D may indicate a constitutive activity, resulting in hyperphosphorylation of Mastl.

Subcellular localization of the ectopic Mastl variants was analyzed by immunocytochemistry staining using anti-Mastl antibodies. As expected, endogenous and ectopic Mastl WT proteins localized to the nucleus. Mastl S861A and S861D mutants also localized to the nucleus (Figure 3(A)). Therefore, S861 phosphorylation has no effect on Mastl localization.

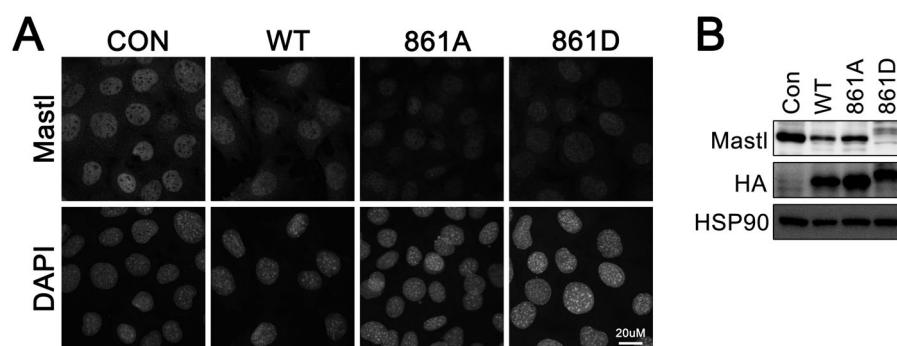


Figure 3. Expression and localization analysis of ectopic Mastl variants. (A) Cells were fixed and stained with anti-Mastl antibodies. Expression levels of Mastl 861A and 861D proteins were lower than the endogenous Mastl (upper panels) but they localized to the nucleus (bottom, DAPI). Scale bar is 20 μ m. (B) Protein extracts from clonal cell lines were analyzed by western blot to compare ectopic Mastl expression to endogenous levels. Expression of the ectopic Mastl protein was lower in all complemented clones.

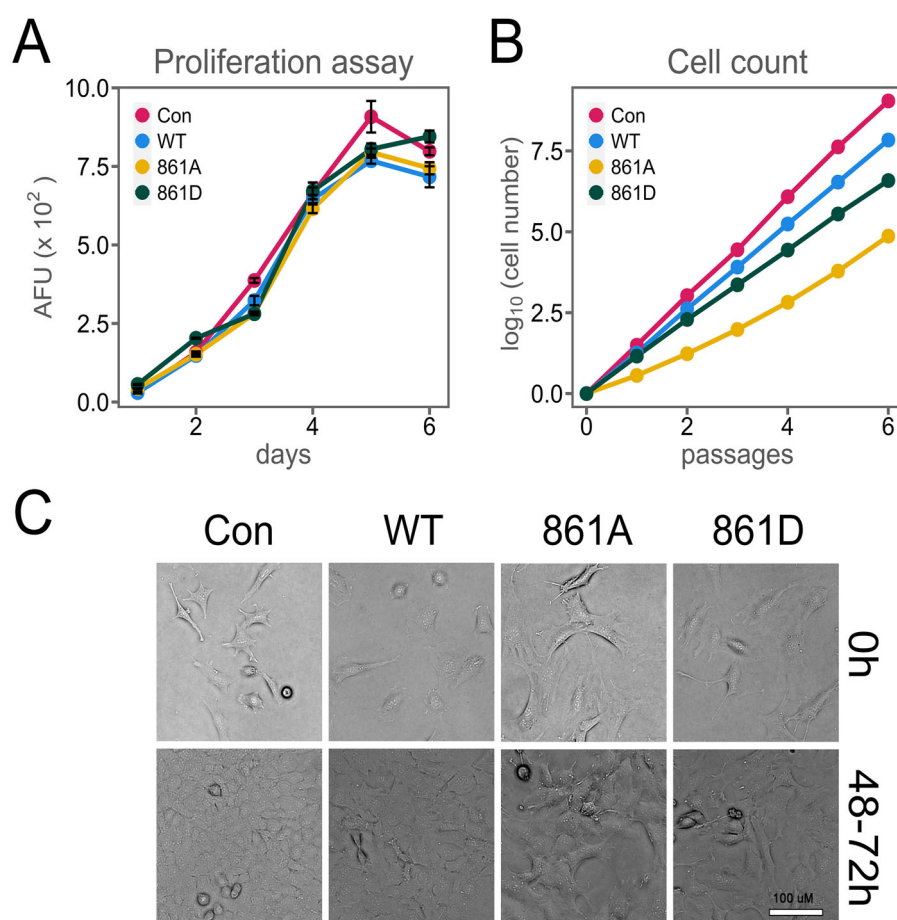


Figure 4. Proliferation rates of control, WT, 861A and 861D clones (A) alamarBlue proliferation assay of the control and clonal cell lines. The metabolic activity was fluorometrically measured as a function of resazurin reduction capacity. The cells were monitored for six days. (AFU: Arbitrary Fluorescence Unit) (B) A modified 3T3 assay was performed to directly measure the increase in cell number over the course of six passages. Number of cells at the beginning of the assay were normalized to one. (C) The cells were seeded at low density in order to show their unique morphologies in the absence of cell–cell contact restrictions (upper row). In a 6-well plate, the semi-confluent asynchronous cells were treated with DMSO or 20 ng/mL 4-OHT. The next day, 20,000 cells/well were seeded. The bright field images were acquired two days later (three days in the case of 861A due to its slower growth rate) (lower row). Scale bar is 100 μ m.

3.3. The Mastl S861 phosphosite mutations do not impair cell proliferation

We have demonstrated that deletion of endogenous Mastl can be rescued when Mastl S861A or Mastl S861D mutants are expressed ectopically. To compare the proliferation rates of these clones to that of control MEFs or Mastl WT-expressing knockout clones, we decided to undertake quantifiable assays.

First, the proliferation rates of these clones were measured indirectly by alamarBlue proliferation assay which measures the overall metabolic activity over time. The results suggest that the mutant Mastl-expressing clonal cell lines have proliferation rates comparable to control cells or Mastl WT clonal cell line (Figure 4(A)). Next, we measured the proliferation rates directly by a modified 3T3 assay (see

Methods). The mutant clones had slightly reduced proliferation rates compared to the control cells or WT clone (Figure 4(B)). We observed that 861A and 861D clones had slightly larger cells compared to parental cells or the WT clone (Figure 4(C)). This finding could be best explained by an increased length of the cell cycle allowing a longer period for cell growth.

These results suggest that, S861 phosphorylation site mutations do not have a lethal negative effect on cell proliferation rate. In fact, the slight reduction in proliferation rates of the mutant clones is possibly due to the lower expression level of ectopic Mastl proteins (See Figure 3). However, reduced kinase activity, especially for the 861A variant cannot be ruled out.

3.4. Mastl kinase C-tail non-phosphorylatable mutant (S861A) is capable of hyperphosphorylation

Xenopus Mastl kinase undergoes hyperphosphorylation during its activation (Blake-Hodek et al., 2012). In mitotically arrested primary MEFs, a slower running phosphorylated isoform appears in immunoblots. The apparent high molecular weight band is due to the decreased electrophoretic mobility of the hyperphosphorylated Mastl protein (Diril et al., 2016).

To investigate whether the hyperphosphorylation can take place in case of C-tail phosphosite-deficient Mastl, we treated the control cells and the ectopic WT Mastl-expressing homozygous knockout clones with nocodazole for different time intervals to arrest cells in mitosis. The Western blots for Mastl protein show that both cell groups display the band upshift (Figure 5(A)). This means that the ectopically expressed wild-type Mastl can complete its phosphorylation-dependent activation.

Next, we asked whether Mastl S861A mutant can become hyperphosphorylated. To that end, we repeated the mitotic arrest and phosphorylation analysis, this time including the 861A clone (Figure 5(B)). It is observed that 861A clone is also capable of phosphorylation. This finding could be corroborated in HEK293T cells transfected with HA-tagged WT or 861A mutant constructs (Figure 5(C)). All in all, these results show that 861A is capable of completing its activation steps, suggested by the mitotic arrest experiments (Figure 5). Which explains why the mutant is able to rescue the cell cycle in Figure 4.

3.5. Conformation of the phosphosite defines the C-tail/N-lobe interactions

Our experimental results suggest that pS861 phosphoresidue is auxiliary for Mastl kinase activation. To mechanistically explain this result, we analyzed the C-tail intramolecular interactions of Mastl and other AGC kinases. Currently, there is only one crystal structure of Mastl (*Homo sapiens*, 5LOH) available in the PDB. Due to solubility issues, the construct was truncated at its NCMR to obtain the minimal kinase domains (Ocasio et al., 2016). Despite the construct contained C-tail of human Mastl, C-tail was not present in the final structure. Because of this, we decided to find suitable

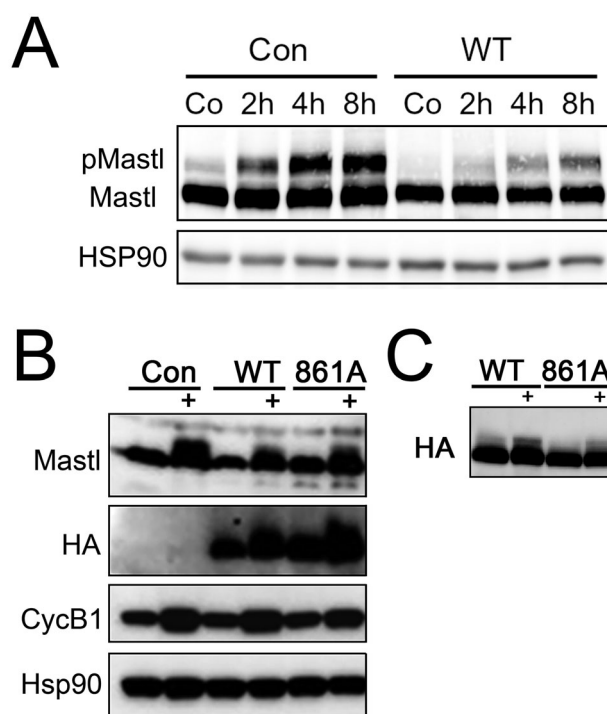


Figure 5. Mastl S861A variant is capable of hyperphosphorylation. (A) Mitotic arrest of asynchronously proliferating primary MEFs results in phosphorylation of Mastl, which can be detected by a higher MW band in western blots. Mitotic arrest was performed for 2, 4 and 8 h. Con indicates the non-transduced control cells. WT indicates the wild-type ectopic Mastl-expressing homozygous knockout clone. Co indicates the untreated asynchronous cells. (B) Control, WT and S861A clonal cell lines were arrested in mitosis and analyzed by WB. Mastl S861A mutant underwent phosphorylation. The blots were immunostained with anti-Mastl and anti-HA antibodies. Cyclin B1 levels were analyzed to show enrichment of mitotic cells after treatment and HSP90 as loading control. (C) HEK293T cells transfected with HA-tagged Mastl WT or 861A were arrested in mitosis by nocodazole treatment (+) for 4 h. Protein extracts of the cells were analyzed by WB using anti-HA antibodies.

templates for homology modeling of Mastl. To this end, we have collected all available AGC kinase crystal structures that possess a phosphorylated C-tail. According to this criterion, 17 structures of two different AGC kinases are available in PDB, which are PKC iota and PKA (Supporting Information Table S1). The structures fall into two distinct groups based on the conformation of their phosphorylated C-tail residue. The phosphoresidue is either buried in N-lobe, or it is solvent-exposed (Supporting Information Figure S3). Upon observing that there are two distinct C-tail phosphoresidue conformations, we first decided to elucidate which conformation would Mastl pS861 possess (buried or solvent-exposed). For this, we performed pairwise sequence alignments between the kinase domains of mouse Mastl and human PKC iota or mouse PKA (Supporting Information Figure S6).

The sequence alignments revealed that mouse Mastl C-tail phosphosite does not correspond to a phosphoresidue in PKA and PKC iota, but it corresponds to an aspartate in PKC iota. To get a detailed insight, we obtained two separate homology models for Mastl, by using PKC iota (3A8W) or PKA (3FJQ) as the templates. Expectedly, the C-tail phosphosite of the model structures possesses the distinct conformation (i.e., solvent-exposed or buried) of their respective templates (Figure 6). Using HADDOCK2.2 web server, the binding score of C-tail to N-lobe was predicted by using van

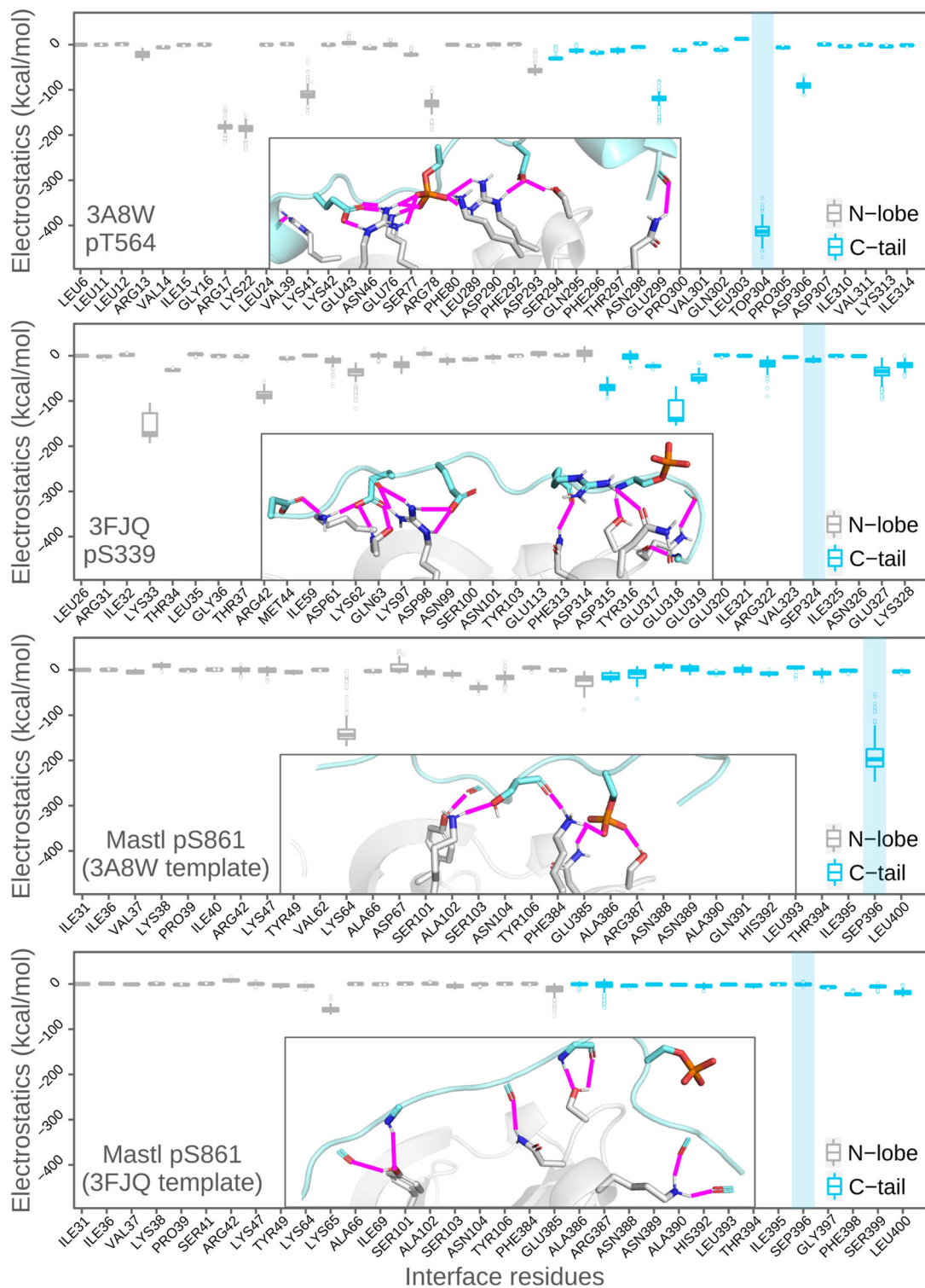


Figure 6. The PKC iota crystal structure (3A8W), PKA crystal structure (3FJQ), mouse Mastl 3A8W-based model structure and mouse Mastl 3FJQ-based model structure were subjected to structural refinement using HADDOCK2.2 web server. For each structure, simulation results of their phosphorylated forms are given. Throughout the energy minimization, HADDOCK generated 200 states for each starting structure. For each interface residue, electrostatics scores of these 200 model structures are given as boxplots. Each box shows the energy distribution of individual residues throughout the simulation. For each run, among the 200 generated model structures, the one that has the lowest (best) HADDOCK score was selected for three-dimensional depiction of the interfaces, given in the respective plot areas. Both in the plots and in the respective structure views, C-tail turn motif and N-lobe are cyan and gray colored, respectively. The transparent blue rectangle on right side of each plot indicates the position of C-tail phosphosite. The interfacial polar contacts were detected by PyMOL. The residues that form polar contacts are depicted as sticks. The polar contacts are depicted as magenta lines. The blue, orange and red colored atoms are nitrogen, phosphorus and oxygen, respectively. Residues are numbered according to their positions within the truncated structures. Positions of the phosphosites within full-length sequences are written in bottom-left corner of each plot.

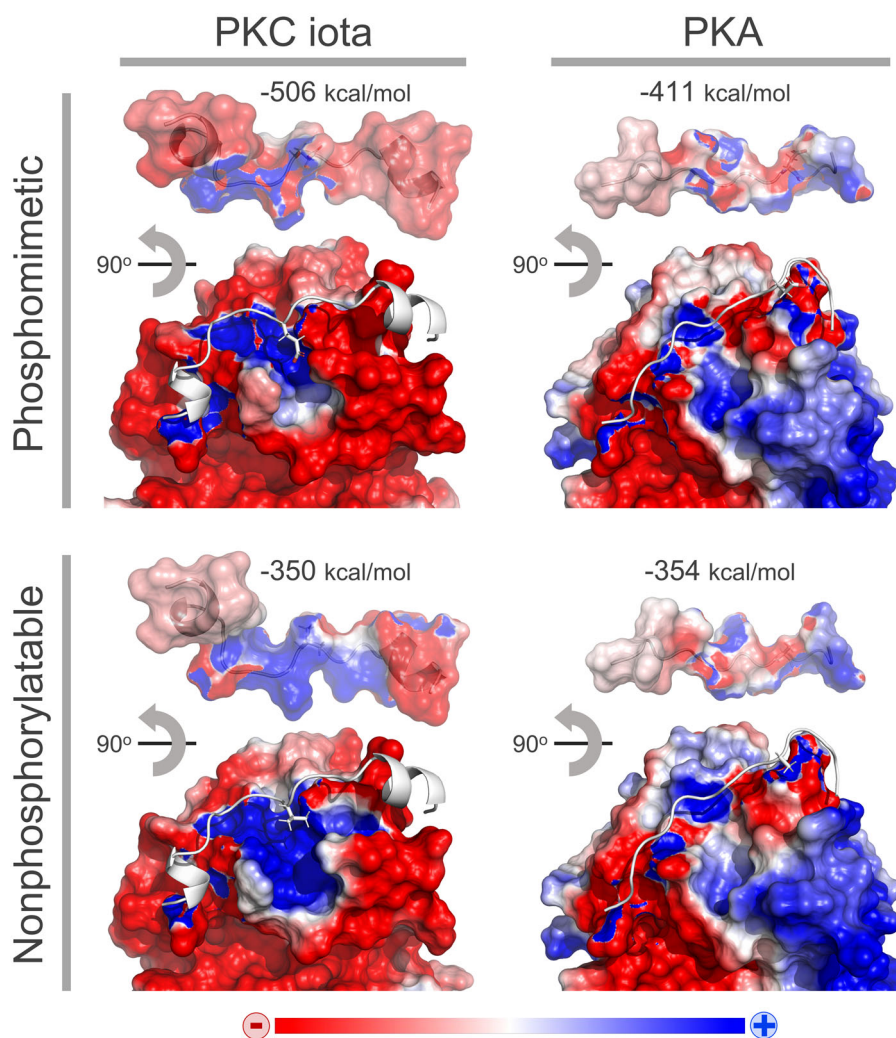


Figure 7. Phosphomimetic (T564E) and nonphosphorylatable (T564V) mutants of PKC iota and phosphomimetic (S339D) and nonphosphorylatable (S339A) mutants of PKA were generated using HADDOCK2.2. For each four mutant, post-simulation structure with the lowest HADDOCK score was subjected to APBS calculations. The surface electrostatics potentials were calculated and mapped onto three-dimensional structures. Red indicates negative potential and blue indicates positive potential. In each structure, C-tail is represented as white cartoon. The 90° rotated state of C-tails are given on top of their respective structures in order to show the surface electrostatics potentials of each interface in detail. The C-tail binding electrostatics scores that were obtained from HADDOCK2.2 are given on top of each structure. Lower electrostatics score corresponds to stronger binding.

der Waals score, electrostatics score, desolvation energy and the combined HADDOCK scoring function (Supporting Information Figure S7). The calculations were performed on nonphosphorylatable, wild-type, phosphomimetic and phosphorylated forms of PDB 3A8W (PKC iota), PDB 3FJQ (PKA), 3A8W-based Mast1 model and 3FJQ-based Mast1 model. Due to the charged interactions between the C-tail phosphoresidue and the N-lobe basic patch residues, we have turned our attention to the electrostatics scores of interfacial residues. As expected, when C-tail phosphoresidue is buried inwards N-lobe, its contribution to the binding energies dramatically increases (Figure 6).

The energetics analyses expectedly verified the notion that when the phosphoresidue is buried, it greatly contributes to the intramolecular interactions and when it is solvent-exposed, it does not. However, intriguingly, the unique patterns of polar contact distribution unveiled that in PKC iota and PKC-iota-based Mast1 model, the contacts are clustered at the center, whereas in case of PKA and PKA-based Mast1 model, the contacts are clustered more at the edges of

the interface (Figure 6). Given that the PKA C-tail phosphoresidue does not contribute to the C-tail docking, this two-sided stitching of its C-tail might be a structural feature that has evolved as a means to promote phosphorylation-independent docking. We then evaluated the structural impacts of nonphosphorylatable or phosphomimetic mutations of C-tail phosphosite. To this end, we selected the HADDOCK-refined structures with the lowest HADDOCK score for the said mutants of PKC iota (based on PDB entry 3A8W) and PKA (based on PDB entry 3FJQ) in order to use for APBS (Adaptive Poisson–Boltzmann Solver) calculations. The surface electrostatics potentials were calculated and mapped onto three-dimensional structures (Figure 7). The electrostatics potential maps show that phosphomimetic glutamate mutation in PKC iota is interacting with basic patch (the blue cavity). When this C-tail phosphosite is mutated into nonphosphorylatable valine, basic patch is expanded. In other words, distance between the edges of basic patch increases. This is because of the fact that, in the absence of a negative charge where there should be the phosphoresidue, basic

patch residues cannot engage in a polar contact network. Conversely, in case of PKA, the phosphomimetic or nonphosphorylatable mutations of C-tail phosphosite do not cause a remarkable structural difference. Because, C-tail phosphosite is already tilted away from N-lobe (Figure 7). These results together reinforce our hypothesis that Mastl pS861 phosphoresidue does not contribute to intramolecular C-tail docking.

4. Conclusion

In AGC kinases, activation loop and C-tail phosphorylations are crucial for kinase activation. Activating phosphorylations govern the conformational transition from inactive to active state through a chain of molecular interactions. One feature that makes Mastl a unique AGC kinase, other than its long NCMR domain, is that, it has an N-lobe hydrophobic groove, yet it is devoid of a hydrophobic motif (HF) (FXXF) to bind it. In other words, Mastl's C-tail is partially missing. Another protein kinase that shares this unique feature is PDK1. PDK1 circumvents this structural shortfall by binding the HF motifs of other AGC kinases to achieve complete activation (Biondi, 2001; Biondi et al., 2000). Consistently, Vigneron et al. (2011) demonstrated that a partially active mutant form of human Mastl (K72M) could achieve 156% of its basal activity in the presence of a synthetic peptide (PIFtide) that contains HF motif. Given the lack of HF motif in Mastl and given that Mastl possibly compensates for this by utilizing the HF motif of other kinases, one cannot directly assign a biological function to its C-tail phosphosite.

Although AGC kinases have been studied for decades, the role of C-tail phosphosite in the final activation step is still a mystery for atypical AGC kinases. To date, several studies have sought to characterize the activation steps of Mastl kinase using different experimental approaches (Blake-Hodek et al., 2012; Hermida et al., 2020; Vigneron et al., 2011). Ultimately, C-tail phosphorylation was proposed to be one of the essential steps for Mastl activation.

Vigneron et al. (2011) used mitotic CSF egg extracts and depleted endogenous *Xenopus* Greatwall kinase which induces mitotic exit (Burgess et al., 2010). They supplemented these extracts with *in vitro*-transcribed human Mastl mRNAs coding for various mutants. The mutants were evaluated for their potential to restore the mitotic state by Western blot analysis of Cdk phosphorylations on mitotic substrates. Additionally, they performed kinase assays to measure kinase activity of recombinant Mastl variants using MBP (myelin basic protein) as substrate. Results from both assays showed that, the activity of 875A mutant (861A in mouse) was significantly reduced (31% of WT activity on MBP). Nonetheless, there was a residual activity compared to the kinase-dead mutant G44S (5% of WT).

Blake-Hodek et al. (2012) essentially used the same experimental methodology. However, they produced the different Mastl mutants (*Xenopus*) by baculovirus infection of Sf9 insect cells. They quantified the kinase activity by measuring Mastl autophosphorylation or using MBP as substrate in kinase assays. They also observed a significant decrease in the

activity of 883A mutant (861A in mouse). Nevertheless, the activity of Mastl 883A mutant was more than the kinase-dead mutant G41S (*Xenopus*).

Finally, in their elaborate phosphoproteomics study aiming to analyze the mechanism of MASTL activation and regulation, Hermida et al. (2020) used recombinant human Mastl kinase (WT or kinase-dead mutant) and mitotic HEK293 cells extracts. They identified the differentially phosphorylated sites between the variants, verifying that S875 is a *cis*-autophosphorylated residue. Although their observations show that S875 phosphorylation occurs on human Mastl, whether it is essential for activity was not investigated.

In this work, we have used Mastl CKO MEFs to remove the endogenous Mastl kinase and sought to rescue its loss by various mutants. The primary readouts of our system, cellular proliferation and autophosphorylation, show that S861 phosphorylation is not essential for activation or mitotic division. The apparent discrepancy between our results and the aforementioned papers could be due to two reasons: (i) The impaired activity of Mastl 861A mutants may be sufficient to drive mammalian cells through mitosis. (ii) *Xenopus* CSF egg extracts constitute a simplified model system and do not fully reflect the elaborate regulatory network responsible for mitotic entry in mammalian cells. Therefore, our model system allows us to functionally characterize the Mastl variants at the level of cell fate and our observations are directly relevant to mitosis.

Taken together, our present results render the generalizability of final step of current AGC kinase activation model (Arencibia et al., 2013; Hauge et al., 2007; Kannan et al., 2007) questionable for AGC kinases that are devoid of an HF motif. We hope that our results encourage researchers in the field to engage in deeper structural and enzymological studies for atypical AGC protein kinases. Conversely, we have demonstrated the complementation cloning strategy as a robust assay that allows cell culture-based mutagenesis screening of essential proteins.

Acknowledgement

We thank Prof. Dr. Philipp Kaldis for sharing the plasmids, cell lines and antibodies used in this study.

Disclosure statement

An earlier version of this work has been published in preprint server bioRxiv.org, Erguven et al., 2020

Funding

This work was supported by Dokuz Eylul University Scientific Research Projects grant (DEU-BAP Project No: 2016.KB.SAG.014). MKD received additional support from Turkish Academy of Sciences (GEBIP award) and The Science Academy, Turkey (BAGEP award). ME was supported by a stipend from TUBITAK (The Scientific and Technological Research Council of Turkey) Project No. 217Z248. EK received support from The Science Academy, Turkey (BAGEP award) and EMBO Installation Grant (no: 4421).

ORCID

Mehmet Erguven  <http://orcid.org/0000-0001-5947-8568>
 Seval Kilic  <http://orcid.org/0000-0001-6735-8996>
 Ezgi Karaca  <http://orcid.org/0000-0002-4926-7991>
 M. Kasim Diril  <http://orcid.org/0000-0002-3644-4178>

Authors' contributions

ME and MKD conceived and designed the project, ME, SK and MKD acquired the data, ME, EK and MKD analyzed and interpreted the data, ME and MKD wrote the paper. All authors contributed to careful revising of the manuscript.

References

- Adams, J. A. (2003). Activation loop phosphorylation and catalysis in protein kinases: Is there functional evidence for the autoinhibitor model? *Biochemistry*, 42(3), 601–607. <https://doi.org/10.1021/bi020617o>
- Alvarez-Fernandez, M., Sanchez-Martinez, R., Sanz-Castillo, B., Gan, P. P., Sanz-Flores, M., Trakala, M., Ruiz-Torres, M., Lorca, T., Castro, A., & Malumbres, M. (2013). Greatwall is essential to prevent mitotic collapse after nuclear envelope breakdown in mammals. *Proceedings of the National Academy of Sciences of the United States of America*, 110(43), 17374–17379. <https://doi.org/10.1073/pnas.1310745110>
- Archambault, V., Zhao, X., White-Cooper, H., Carpenter, A. T. C., & Glover, D. M. (2007). Mutations in drosophila greatwall/scant reveal its roles in mitosis and meiosis and interdependence with polo kinase. *PLoS Genetics*, 3(11), e200. <https://doi.org/10.1371/journal.pgen.0030200>
- Arencibia, J. M., Fröhner, W., Krupa, M., Pastor-Flores, D., Merker, P., Oellerich, T., Neimanis, S., Schmithals, C., Köberle, V., Süß, E., Zeuzem, S., Stark, H., Piiper, A., Odadzic, D., Schulze, J. O., & Biondi, R. M. (2017). An allosteric inhibitor scaffold targeting the PIF-pocket of atypical protein kinase C isoforms. *ACS Chemical Biology*, 12(2), 564–573. <https://doi.org/10.1021/acscchembio.6b00827>
- Arencibia, J. M., Pastor-Flores, D., Bauer, A. F., Schulze, J. O., & Biondi, R. M. (2013). AGC protein kinases: From structural mechanism of regulation to allosteric drug development for the treatment of human diseases. *Biochimica et Biophysica Acta*, 1834(7), 1302–1321. <https://doi.org/10.1016/j.bbapap.2013.03.010>
- Baker, N. A., Sept, D., Joseph, S., Holst, M. J., & McCammon, J. A. (2001). Electrostatics of nanosystems: Application to microtubules and the ribosome. *Proceedings of the National Academy of Sciences of the United States of America*, 98(18), 10037–10041. <https://doi.org/10.1073/pnas.181342398>
- Berman, H. M., Westbrook, J., Feng, Z., Gilliland, G., Bhat, T. N., Weissig, H., Shindyalov, I. N., & Bourne, P. E. (2000). The protein data bank. *Nucleic Acids Research*, 28(1), 235–242. <https://doi.org/10.1093/nar/28.1.235>
- Biondi, R. M., Cheung, P. C. F., Casamayor, A., Deak, M., Currie, R. A., & Alessi, D. R. (2000). Identification of a pocket in the PDK1 kinase domain that interacts with PIF and the C-terminal residues of PKA. *The EMBO Journal*, 19(5), 979–988. <https://doi.org/10.1093/emboj/19.5.979>
- Biondi, R. M., Kieloch, A., Currie, R. A., Deak, M., & Alessi, D. R. (2001). The PIF-binding pocket in PDK1 is essential for activation of S6K and SGK, but not PKB. *The EMBO Journal*, 20(16), 4380–4390. <https://doi.org/10.1093/emboj/20.16.4380>
- Bisteau, X., Lee, J., Srinivas, V., Lee, J. H. S., Niska-Blakie, J., Tan, G., Yap, S. Y. X., Hom, K. W., Wong, C. K., Chae, J., Wang, L. C., Kim, J., Rancati, G., Sobota, R. M., Tan, C. S. H., & Kaldis, P. (2020). The Greatwall kinase safeguards the genome integrity by affecting the kinase activity in mitosis. *Oncogene*, 39(44), 6816–6840. <https://doi.org/10.1038/s41388-020-01470-1>
- Blake-Hodek, K. A., Williams, B. C., Zhao, Y., Castilho, P. V., Chen, W., Mao, Y., Yamamoto, T. M., & Goldberg, M. L. (2012). Determinants for activation of the atypical AGC kinase greatwall during M phase entry. *Molecular and Cellular Biology*, 32(8), 1337–1353. <https://doi.org/10.1128/MCB.06525-11>
- Burgess, A., Vigneron, S., Brioudes, E., Labbé, J.-C., Lorca, T., & Castro, A. (2010). Loss of human Greatwall results in G2 arrest and multiple mitotic defects due to deregulation of the cyclin B-Cdc2/PP2A balance. *Proceedings of the National Academy of Sciences of the United States of America*, 107(28), 12564–12569. <https://doi.org/10.1073/pnas.0914191107>
- Das, A., Gerlits, O., Parks, J. M., Langan, P., Kovalevsky, A., & Heller, W. T. (2015). Protein Kinase A Catalytic Subunit Primed for Action: Time-Lapse Crystallography of Michaelis Complex Formation. *Structure (London, England : 1993)*, 23(12), 2331–2340. <https://doi.org/10.1016/j.str.2015.10.005>
- Diril, M. K., Bisteau, X., Kitagawa, M., Caldez, M. J., Wee, S., Gunaratne, J., Lee, S. H., & Kaldis, P. (2016). Loss of the Greatwall kinase weakens the spindle assembly checkpoint. *PLoS Genetics*, 12(9), e1006310. <https://doi.org/10.1371/journal.pgen.1006310>
- Diril, M. K., Ratnacaram, C. K., Padmakumar, V. C., Du, T., Wasser, M., Coppola, V., Tessarollo, L., & Kaldis, P. (2012). Cyclin-dependent kinase 1 (Cdk1) is essential for cell division and suppression of DNA re-replication but not for liver regeneration. *Proceedings of the National Academy of Sciences of the United States of America*, 109(10), 3826–3831. <https://doi.org/10.1073/pnas.1115201109>
- Dolinsky, T. J., Nielsen, J. E., McCammon, J. A., & Baker, N. A. (2004). PDB2PQR: An automated pipeline for the setup of Poisson-Boltzmann electrostatics calculations. *Nucleic Acids Research*, 32, W665–W667. <https://doi.org/10.1093/nar/gkh381>
- Endicott, J. A., Noble, M. E. M., & Johnson, L. N. (2012). The structural basis for control of eukaryotic protein kinases. *Annual Review of Biochemistry*, 81(1), 587–613. <https://doi.org/10.1146/annurev-biochem-052410-090317>
- Erguven, M., Karakulak, T., Diril, M. K., & Karaca, E. (2021). How Far Are We from the Rapid Prediction of Drug Resistance Arising Due to Kinase Mutations?. *ACS Omega*, 6(2), 1254–1265. <https://doi.org/10.1021/acsomega.0c04672>
- Erguven, M., Karaca, E. and Diril MK. (2020). Complementation cloning identifies the essentials of mammalian Mastl kinase activation. *bioRxiv* doi: [10.1101/2020.06.30.179580](https://doi.org/10.1101/2020.06.30.179580)
- Erguven, M., & Karaca, E. (2021). *MehmetErguven/MODOMAX: MODOMAX initial release (v1.0.0)*. Zenodo. <https://doi.org/10.5281/zenodo.4446232>
- Fiser, A., Do, R. K. G., & Šali, A. (2000). Modeling of loops in protein structures. *Protein Science*, 9(9), 1753–1773. <https://doi.org/10.1110/ps.9.9.1753>
- Gharbi-Ayachi, A., Labbé, J. C., Burgess, A., Vigneron, S., Strub, J. M., Brioudes, E., Van-Dorselaer, A., Castro, A., & Lorca, T. (2010). The substrate of Greatwall kinase, Arpp19, controls mitosis by inhibiting protein phosphatase 2A. *Science (New York, N.Y.)*, 330(6011), 1673–1677. <https://doi.org/10.1126/science.1197048>
- Hauge, C., Antal, T. L., Hirschberg, D., Doehn, U., Thorup, K., Idrissova, L., Hansen, K., Jensen, O. N., Jørgensen, T. J., Biondi, R. M., & Frödin, M. (2007). Mechanism for activation of the growth factor-activated AGC kinases by turn motif phosphorylation. *The EMBO Journal*, 26(9), 2251–2261. <https://doi.org/10.1038/sj.emboj.7601682>
- Hermida, D., Mortuza, G. B., Pedersen, A.-K., Pozdnyakova, I., Nguyen, T. T. N., Maroto, M., Williamson, M., Ebersole, T., Cazzamali, G., Rand, K., Olsen, J. V., Malumbres, M., & Montoya, G. (2020). Molecular Basis of the Mechanisms Controlling MASTL. *Molecular & Cellular Proteomics*, 19(2), 326–343. <https://doi.org/10.1074/mcp.RA119.001879>
- Hurtado, B., Trakala, M., Ximénez-Embún, P., El Bakkali, A., Partida, D., Sanz-Castillo, B., Álvarez-Fernández, M., Maroto, M., Sánchez-Martínez, R., Martínez, L., Muñoz, J., García de Frutos, P., & Malumbres, M. (2018). Thrombocytopenia-associated mutations in Ser/Thr kinase MASTL deregulate actin cytoskeletal dynamics in platelets. *The Journal of Clinical Investigation*, 128(12), 5351–5367. <https://doi.org/10.1172/JCI121876>
- Huse, M., & Kuriyan, J. (2002). The conformational plasticity of protein kinases. *Cell*, 109(3), 275–282. [https://doi.org/10.1016/S0092-8674\(02\)00741-9](https://doi.org/10.1016/S0092-8674(02)00741-9)
- Kannan, N., Haste, N., Taylor, S. S., & Neuwald, A. F. (2007). The hallmark of AGC kinase functional divergence is its C-terminal tail, a cis-acting

- regulatory module. *Proceedings of the National Academy of Sciences of the United States of America*, 104(4), 1272–1277. <https://doi.org/10.1073/pnas.0610251104>
- Kassambara, A. (2019). *ggpubr: "ggplot2" Based Publication Ready Plots*. <https://CRAN.R-project.org/package=ggpubr>
- Kim, H., Fernandes, G., & Lee, C. (2016). Protein phosphatases involved in regulating mitosis: Facts and hypotheses. *Molecules and Cells*, 39(9), 654–662. <https://doi.org/10.14348/molcells.2016.0214>
- Kim, M.-Y., Bucciarelli, E., Morton, D. G., Williams, B. C., Blake-Hodek, K., Pellacani, C., Von Stetina, J. R., Hu, X., Somma, M. P., Drummond-Barbosa, D., & Goldberg, M. L. (2012). Bypassing the Greatwall–endosulfine pathway: Plasticity of a pivotal cell-cycle regulatory module in *Drosophila melanogaster* and *Caenorhabditis elegans*. *Genetics*, 191(4), 1181–1197. <https://doi.org/10.1534/genetics.112.140574>
- Kishimoto, T. (2015). Entry into mitosis: A solution to the decades-long enigma of MPF. *Chromosoma*, 124(4), 417–428. <https://doi.org/10.1007/s00412-015-0508-y>
- Martí-Renom, M. A., Stuart, A. C., Fiser, A., Sánchez, R., Melo, F., & Šali, A. (2000). Comparative protein structure modeling of genes and genomes. *Annual Review of Biophysics and Biomolecular Structure*, 29(1), 291–325. <https://doi.org/10.1146/annurev.biophys.29.1.291>
- Mochida, S., & Hunt, T. (2012). Protein phosphatases and their regulation in the control of mitosis. *EMBO Reports*, 13(3), 197–203. <https://doi.org/10.1038/embor.2011.263>
- Mochida, S., Maslen, S. L., Skehel, M., & Hunt, T. (2010). Greatwall phosphorylates an inhibitor of protein phosphatase 2A that is essential for mitosis. *Science (New York, N.Y.)*, 330(6011), 1670–1673. <https://doi.org/10.1126/science.1195689>
- Modi, V., & Dunbrack, R. L. (2019). Defining a new nomenclature for the structures of active and inactive kinases. *Proceedings of the National Academy of Sciences of the United States of America*, 116(14), 6818–6827. <https://doi.org/10.1073/pnas.1814279116>
- Ocasio, C. A., Rajasekaran, M. B., Walker, S., Le Grand, D., Spencer, J., Pearl, F. M. G., Ward, S. E., Savic, V., Pearl, L. H., Hochegger, H., & Oliver, A. W. (2016). A first generation inhibitor of human Greatwall kinase, enabled by structural and functional characterisation of a minimal kinase domain construct. *Oncotarget*, 7(44), 71182–71197. <https://doi.org/10.18632/oncotarget.11511>
- R Core Team. (2019). *R: A language and environment for statistical computing*. R Foundation for Statistical Computing. <https://www.R-project.org/>
- Rice, P. (2000). *EMBOSS: The European Molecular Biology Open Software Suite 2*.
- RStudio Team. (2015). *RStudio: Integrated development environment for R*. RStudio, Inc. <http://www.rstudio.com/>
- Šali, A., & Blundell, T. L. (1993). Comparative protein modelling by satisfaction of spatial restraints. *Journal of Molecular Biology*, 234(3), 779–815. <https://doi.org/10.1006/jmbi.1993.1626>
- Santamaría, D., Barrière, C., Cerqueira, A., Hunt, S., Tardy, C., Newton, K., Cáceres, J. F., Dubus, P., Malumbres, M., & Barbacid, M. (2007). Cdk1 is sufficient to drive the mammalian cell cycle. *Nature*, 448(7155), 811–815. <https://doi.org/10.1038/nature06046>
- Schrödinger LLC. (2015). *The PyMOL Molecular Graphics System, Version 1.8*.
- Slupe, A. M., Merrill, R. A., & Strack, S. (2011). Determinants for substrate specificity of protein phosphatase 2A. *Enzyme Research*, 2011, 398751–398758. <https://doi.org/10.4061/2011/398751>
- Takimura, T., Kamata, K., Fukasawa, K., Ohsawa, H., Komatani, H., Yoshizumi, T., Takahashi, I., Kotani, H., & Iwasawa, Y. (2010). Structures of the PKC- ζ kinase domain in its ATP-bound and apo forms reveal defined structures of residues 533–551 in the C-terminal tail and their roles in ATP binding. *Acta Crystallographica. Section D, Biological Crystallography*, 66(Pt 5), 577–583. <https://doi.org/10.1107/S0907444910005639>
- The GIMP Development Team. (2019). *GIMP (2.10.12)*. <https://www.gimp.org>
- The UniProt Consortium. (2019). UniProt: A worldwide hub of protein knowledge. *Nucleic Acids Research*, 47(D1), D506–D515. <https://doi.org/10.1093/nar/gky1049>
- Truett, G. E., Heeger, P., Mynatt, R. L., Truett, A. A., Walker, J. A., & Warman, M. L. (2000). Preparation of PCR-quality mouse genomic DNA with hot sodium hydroxide and tris (HotSHOT). *BioTechniques*, 29(1), 52–54. <https://doi.org/10.2144/00291bm09>
- van Zundert, G. C. P., Rodrigues, J. P. G., L., M., Trellet, M., Schmitz, C., Kastrius, P. L., Karaca, E., Melquiond, A., S. J., van Dijk, M., de Vries, S. J., Bonvin, & A., M. J. J. (2016). The HADDOCK2.2 web server: User-friendly integrative modeling of biomolecular complexes. *Journal of Molecular Biology*, 428(4), 720–725. <https://doi.org/10.1016/j.jmb.2015.09.014>
- Vigneron, S., Gharbi-Ayachi, A., Raymond, A.-A., Burgess, A., Labbe, J.-C., Labesse, G., Monsarrat, B., Lorca, T., & Castro, A. (2011). Characterization of the mechanisms controlling Greatwall activity. *Molecular and Cellular Biology*, 31(11), 2262–2275. <https://doi.org/10.1128/MCB.00753-10>
- Vijayan, R. S. K., He, P., Modi, V., Duong-Ly, K. C., Ma, H., Peterson, J. R., Dunbrack, R. L., & Levy, R. M. (2015). Conformational analysis of the DFG-out kinase motif and biochemical profiling of structurally validated type II inhibitors. *Journal of Medicinal Chemistry*, 58(1), 466–479. <https://doi.org/10.1021/jm501603h>
- Webb, B., & Šali, A. (2016). Comparative protein structure modeling using MODELLER. *Current Protocols in Bioinformatics*, 54(1), 5.6.1–5.6.37. <https://doi.org/10.1002/cpbi.3>
- Yu, J., Fleming, S. L., Williams, B., Williams, E. V., Li, Z., Somma, P., Rieder, C. L., & Goldberg, M. L. (2004). Greatwall kinase. *The Journal of Cell Biology*, 164(4), 487–492. <https://doi.org/10.1083/jcb.200310059>
- Zheng, J., Trafny, E. A., Knighton, D. R., Xuong, N., Taylor, S. S., Ten Eyck, L. F., & Sowadski, J. M. (1993). 2.2Å refined crystal structure of the catalytic subunit of cAMP-dependent protein kinase complexed with MnATP and a peptide inhibitor. *Acta Crystallographica. Section D, Biological Crystallography*, 49(Pt 3), 362–365. <https://doi.org/10.1107/S0907444993000423>
- Zhong, Z. A., Sun, W., Chen, H., Zhang, H., Lay, E., Lane, N. E., & Yao, W. (2015). Optimizing tamoxifen-inducible Cre/loxP system to reduce tamoxifen effect on bone turnover in long bones of young mice. *Bone*, 81, 614–619. [10.1016/j.bone.2015.07.034](https://doi.org/10.1016/j.bone.2015.07.034) 26232373
- Zhou, T., Commodore, L., Huang, W.-S., Wang, Y., Sawyer, T. K., Shakespeare, W. C., Clackson, T., Zhu, X., & Dalgarno, D. C. (2010). Structural analysis of DFG-in and DFG-out dual Src-Abl inhibitors sharing a common vinyl purine template. *Chemical Biology & Drug Design*, 75(1), 18–28. <https://doi.org/10.1111/j.1747-0285.2009.00905.x>

Supplementary Figures and Tables

Genetic complementation screening and molecular docking give new insight on phosphorylation-dependent Mastl kinase activation

Mehmet Erguven^{1,2}, Seval Kilic^{1,2}, Ezgi Karaca^{1,2}, M. Kasim Diril^{1,2,3*}

¹Izmir Biomedicine and Genome Center, Izmir, Turkey

²Izmir International Biomedicine and Genome Institute, Dokuz Eylul University, Izmir, Turkey

³Department of Medical Biology, Faculty of Medicine, Dokuz Eylul University, Izmir, Turkey

***Corresponding Author:**

E-mail: kasim.diril@ibg.edu.tr

KEYWORDS

Mastl, kinase activation, phosphorylation, cell cycle, HADDOCK

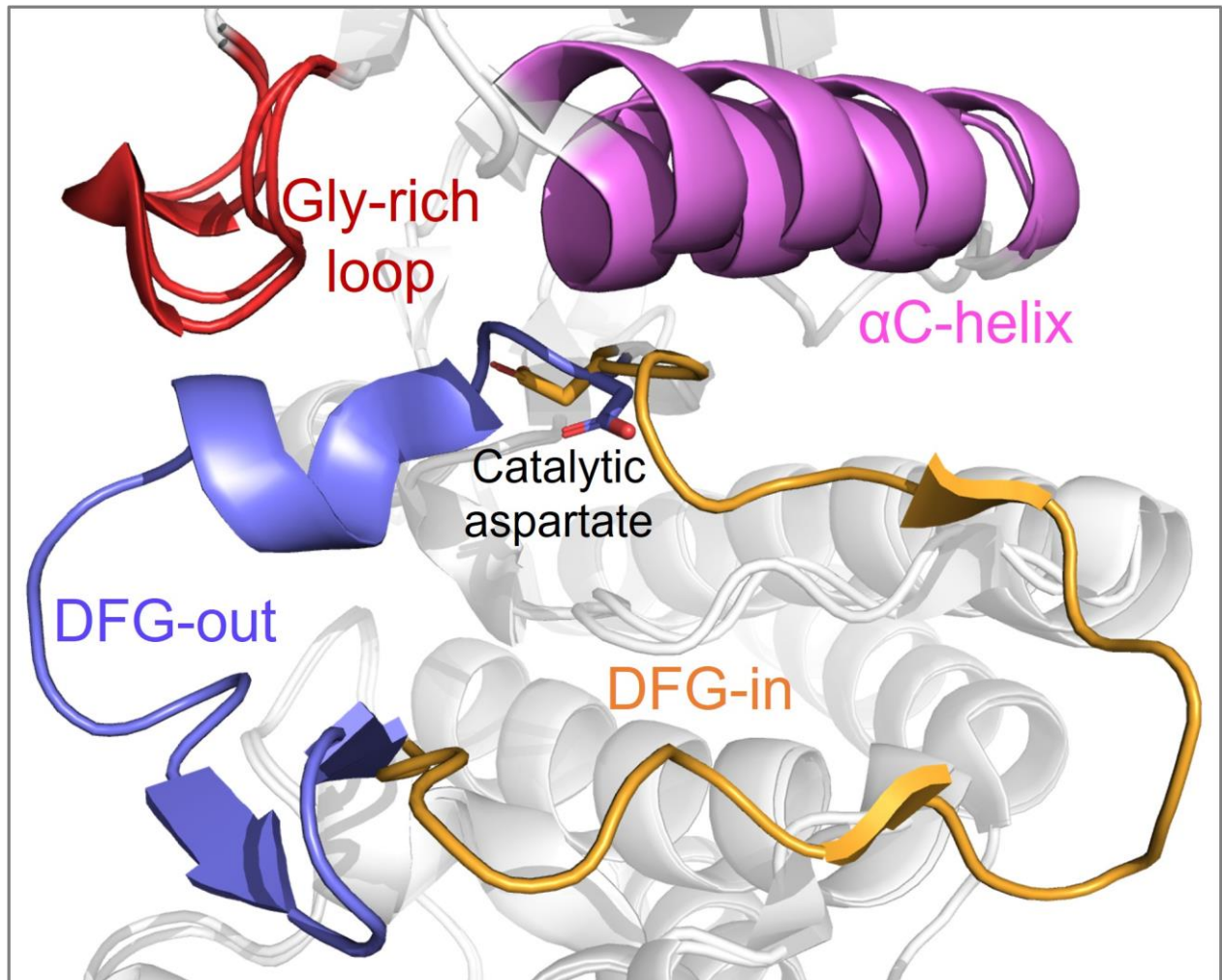


Figure S1. The structural organization of protein kinases. The catalytically important segments; glycine-rich loop (red), activation loop (DFG-out is purple, DFG-in is orange), and α C-helix (pink) are represented. DFG-in and DFG-out conformations of Abl kinase were superposed (PDB entries 3KF4 and 3KFA, respectively) (Zhou et al., 2010).

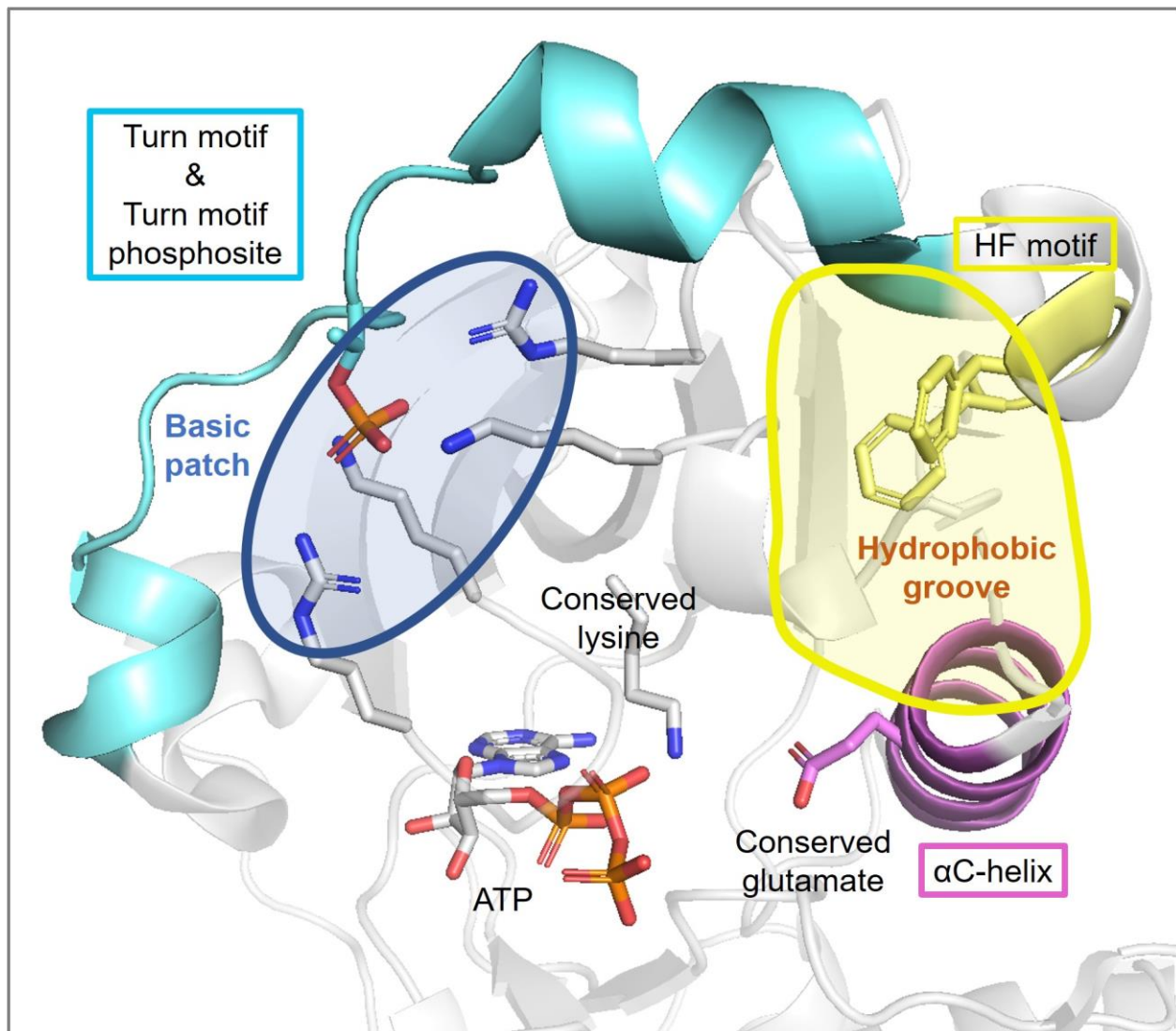


Figure S2. The crystal structure of ATP-bound human PKC iota (PDB entry 3A8W) (Takimura et al., 2010). In the N-lobe the phosphoresidue, conserved lysine and glutamate, the HF motif conserved phenylalanine residues, and the residues that form the basic patch are shown in stick forms. The blue, orange, and red colored atoms are nitrogen, phosphorus, and oxygen, respectively. The basic patch and the hydrophobic groove are indicated by the transparent blue and yellow areas, respectively. The turn motif is cyan colored. The α C-helix (magenta), HF motif (yellow), and the proximal β -strand (transparent gray) together form the hydrophobic groove.

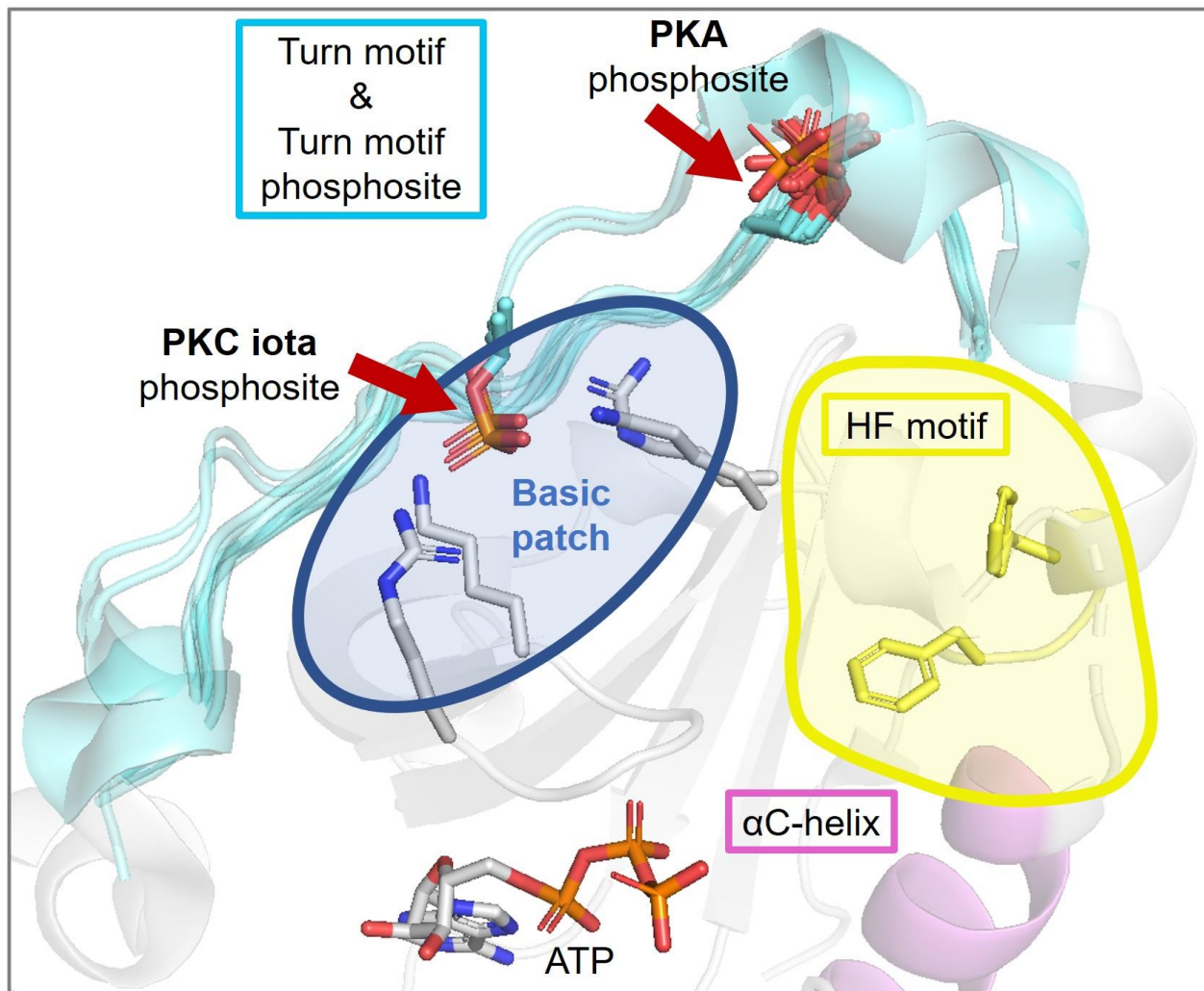


Figure S3. A total of 17 AGC kinase structures were obtained from the PDB and superposed in PyMOL. Among the structures, 2 of them are PKC iota and 15 of them are PKA. The C-tail phosphosite is buried in PKC iota structures while it is solvent exposed in PKA structures. Basic patch is indicated only for one representative PKC iota structure (3A8W). PKA does not possess a corresponding basic patch at its N-lobe surface. The phosphoresidues, basic patch residues, and the HF motif conserved phenylalanine residues are shown in stick forms. The blue, orange, and red colored atoms are nitrogen, phosphorus, and oxygen, respectively. The basic patch and the hydrophobic groove are indicated by the transparent blue and yellow areas, respectively. The turn motif, HF motif, and α C-helix are cyan, yellow, and magenta colored respectively.

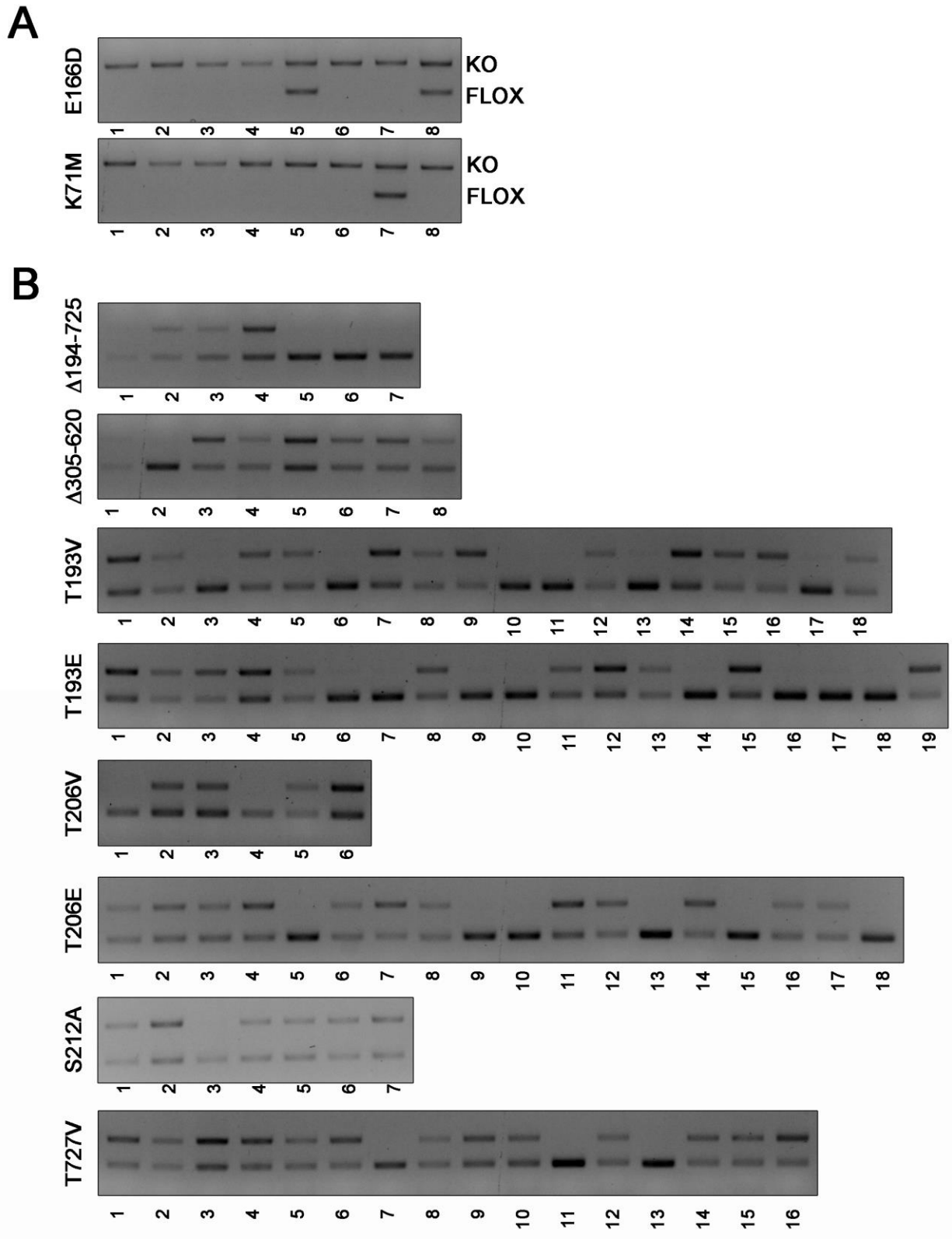


Figure S4. Genotype analysis of clonal cell lines expressing different Mastl mutants. After limited dilution, clonal cell lines were generated and analyzed as explained in Figure 2.

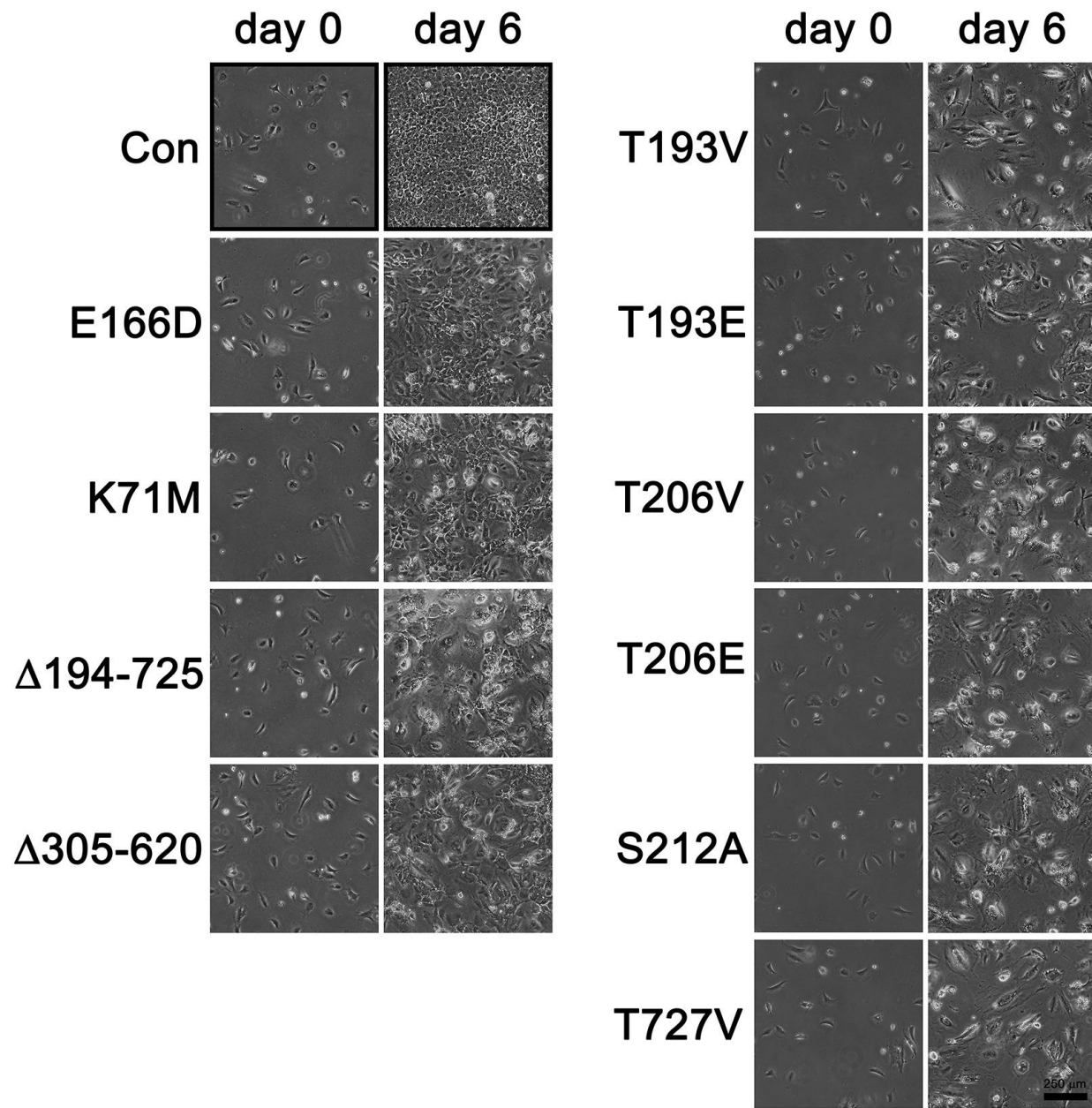
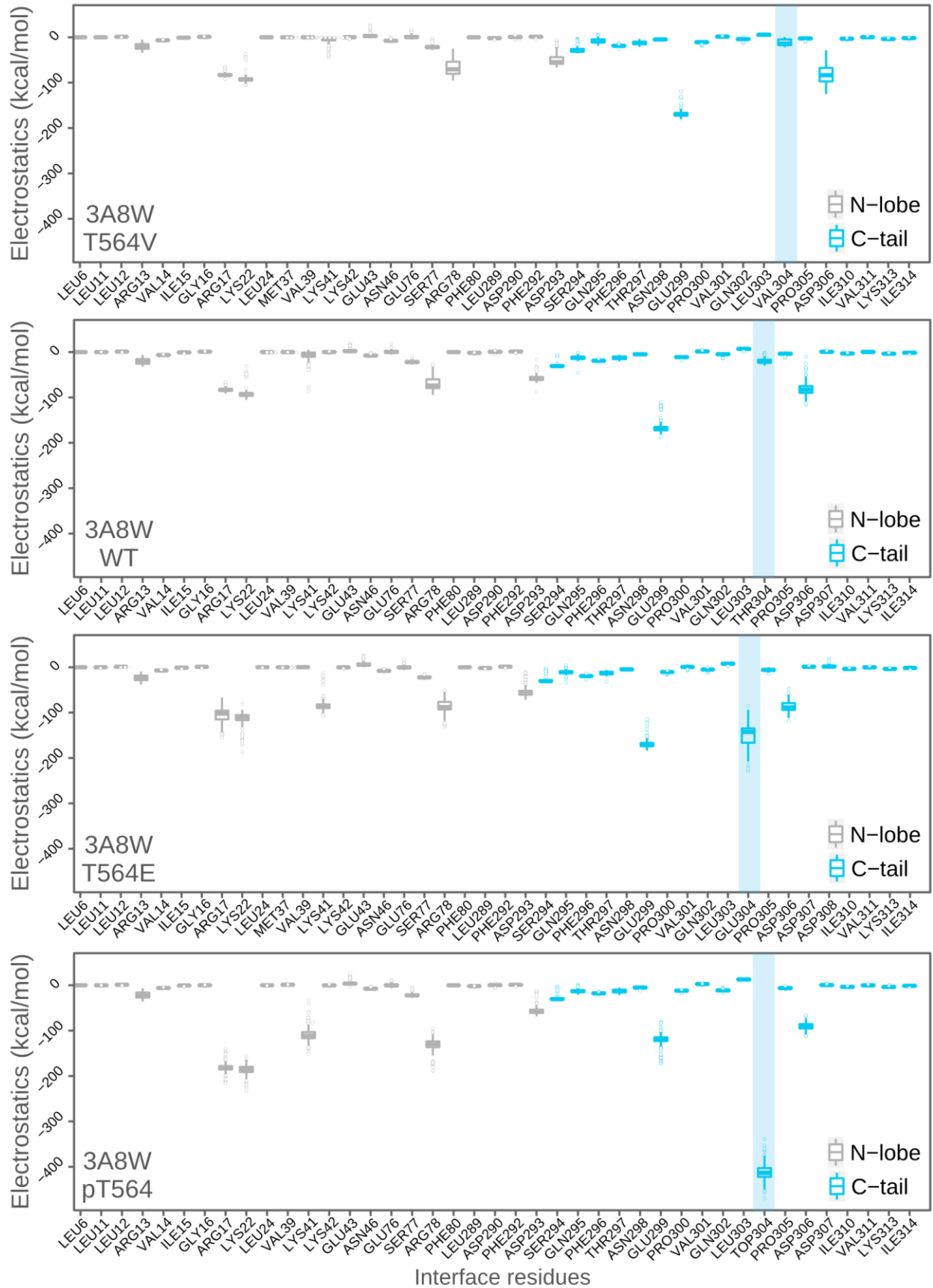
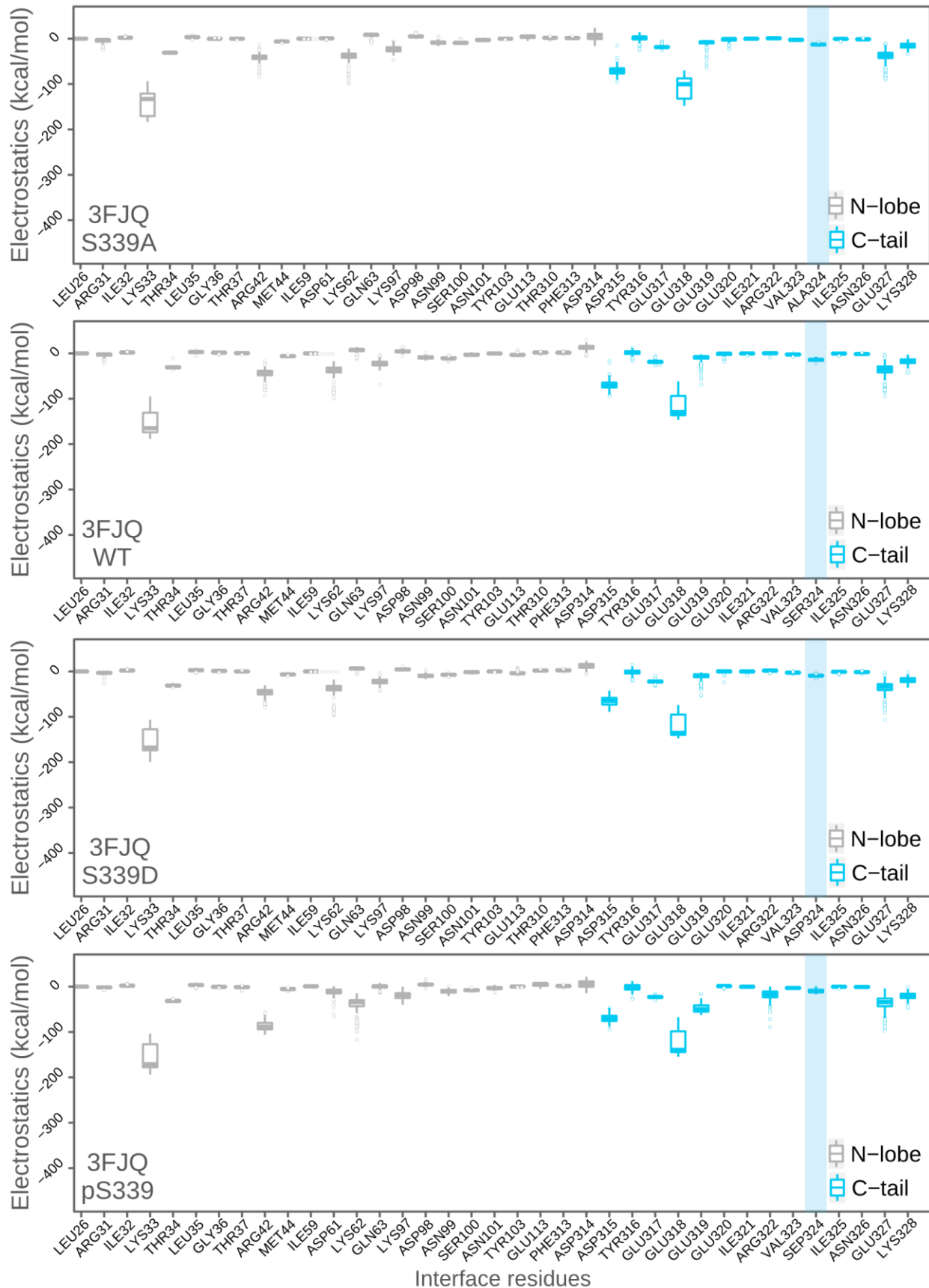


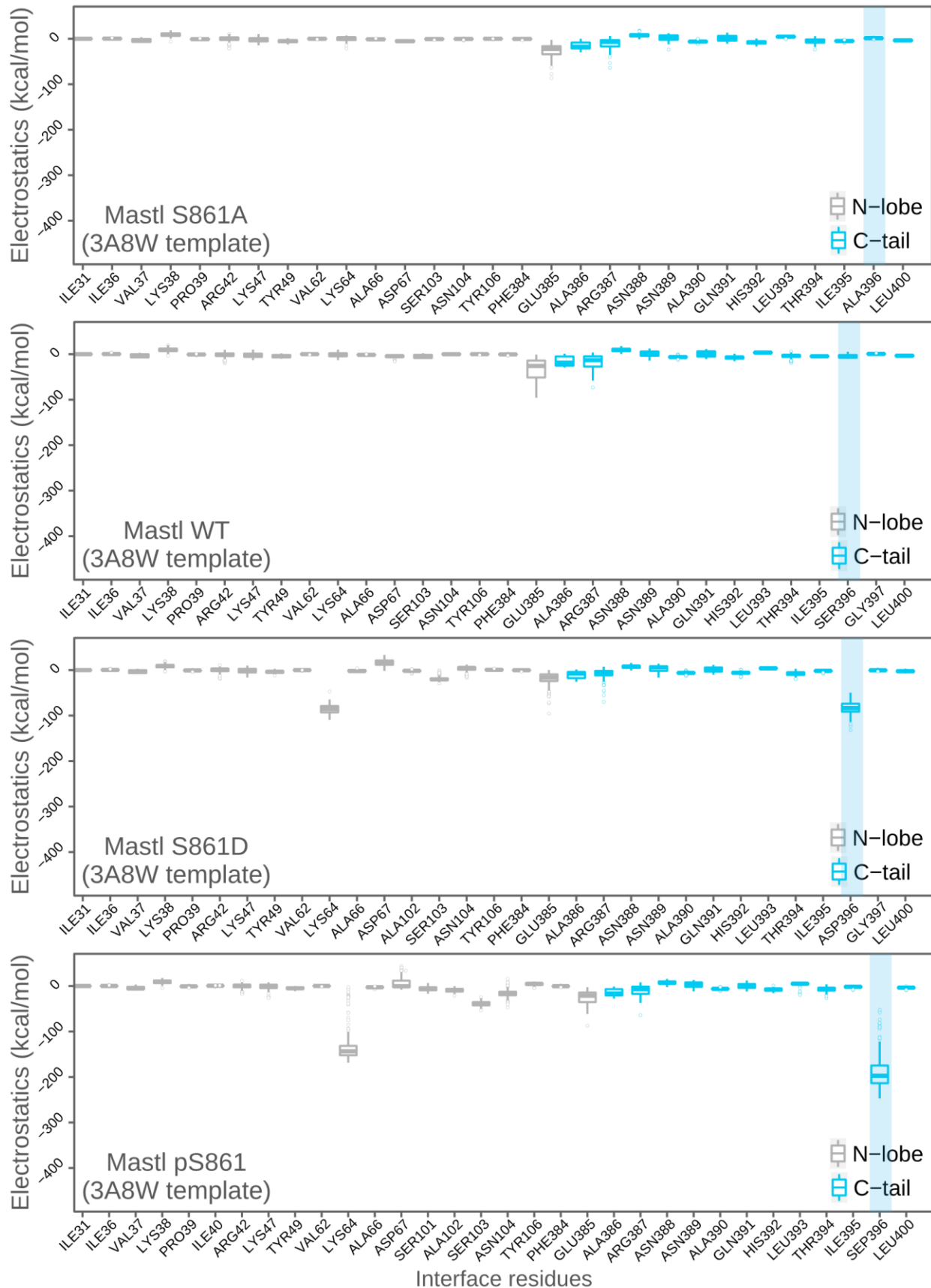
Figure S5. Proliferation of stable cell pools after deletion of endogenous Mastl. The micrographs were acquired immediately before (day 0) and six days (day 6) after 4-OHT treatment. Scale bar is 250 μ m. Con indicates untreated cells.

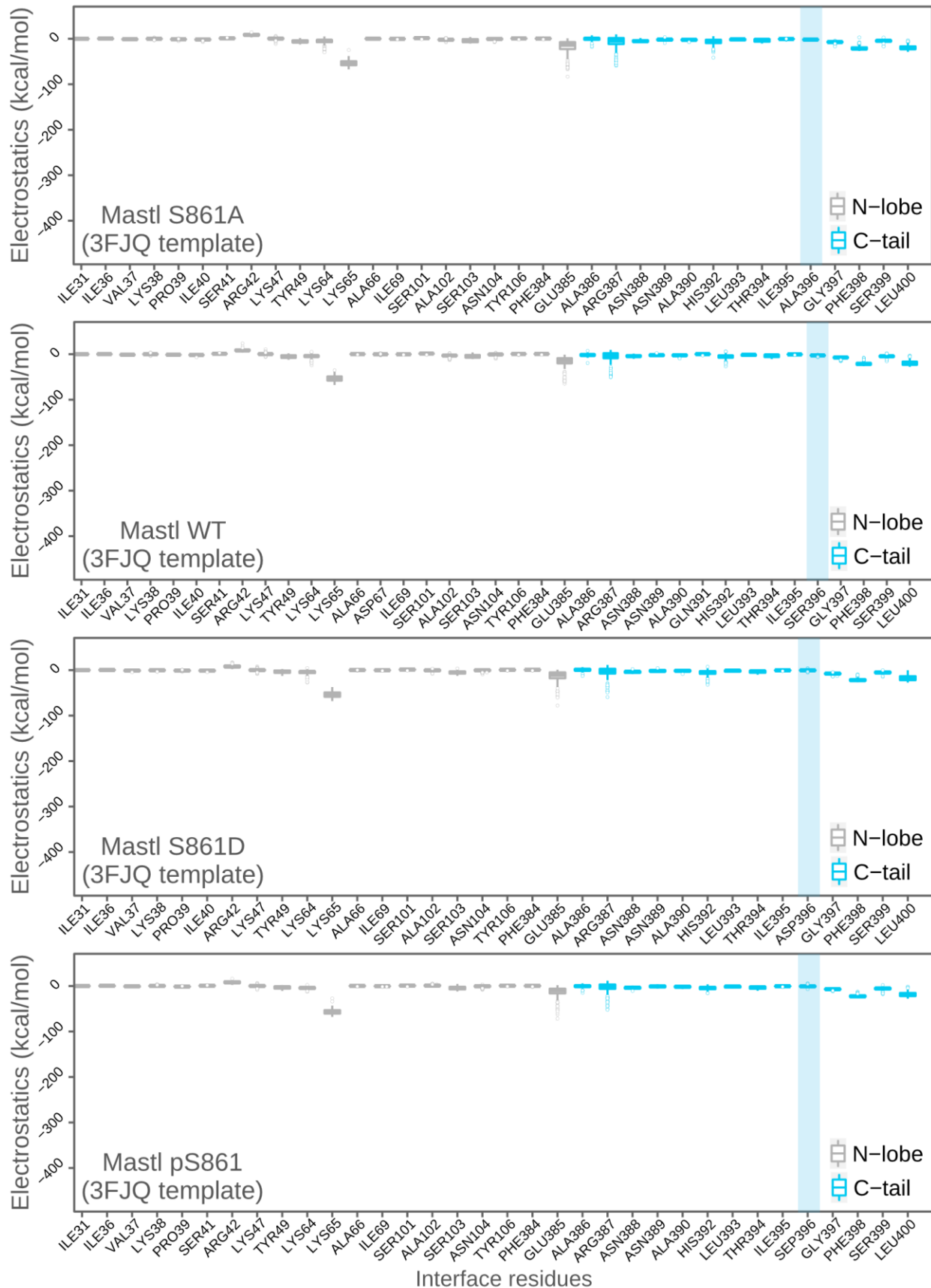
MastI	388	NNAQHLLTISGFSL-----	400
	:	
PKC iota	298	NEPVQLTPDDDDIVRKIDQSEFEGFEYINPL	328
MastI	381	TSYFEARNNAQHLLTISGFSL-----	400
		. :..... :.:.: :	
PKA	310	TSNFDDYEE-EEIRV--SINEKCGKEFTEF	336

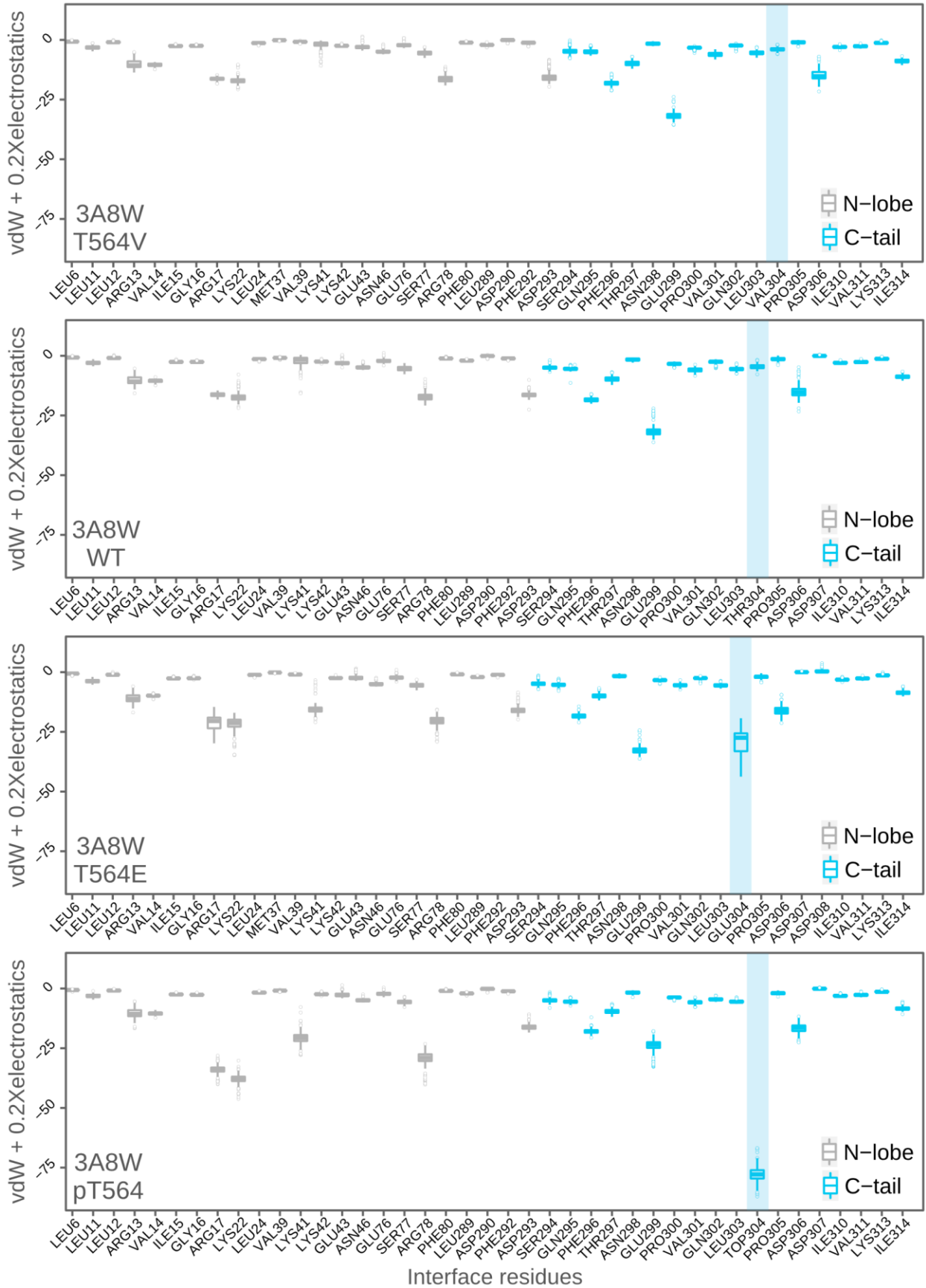
Figure S6. Pairwise sequence alignment of the kinase domains of mouse MastI and human PKC iota or mouse PKA. The alignments were performed by using EMBOSS NEEDLE web server. The NCMR region of MastI was omitted from the sequence prior to alignment.

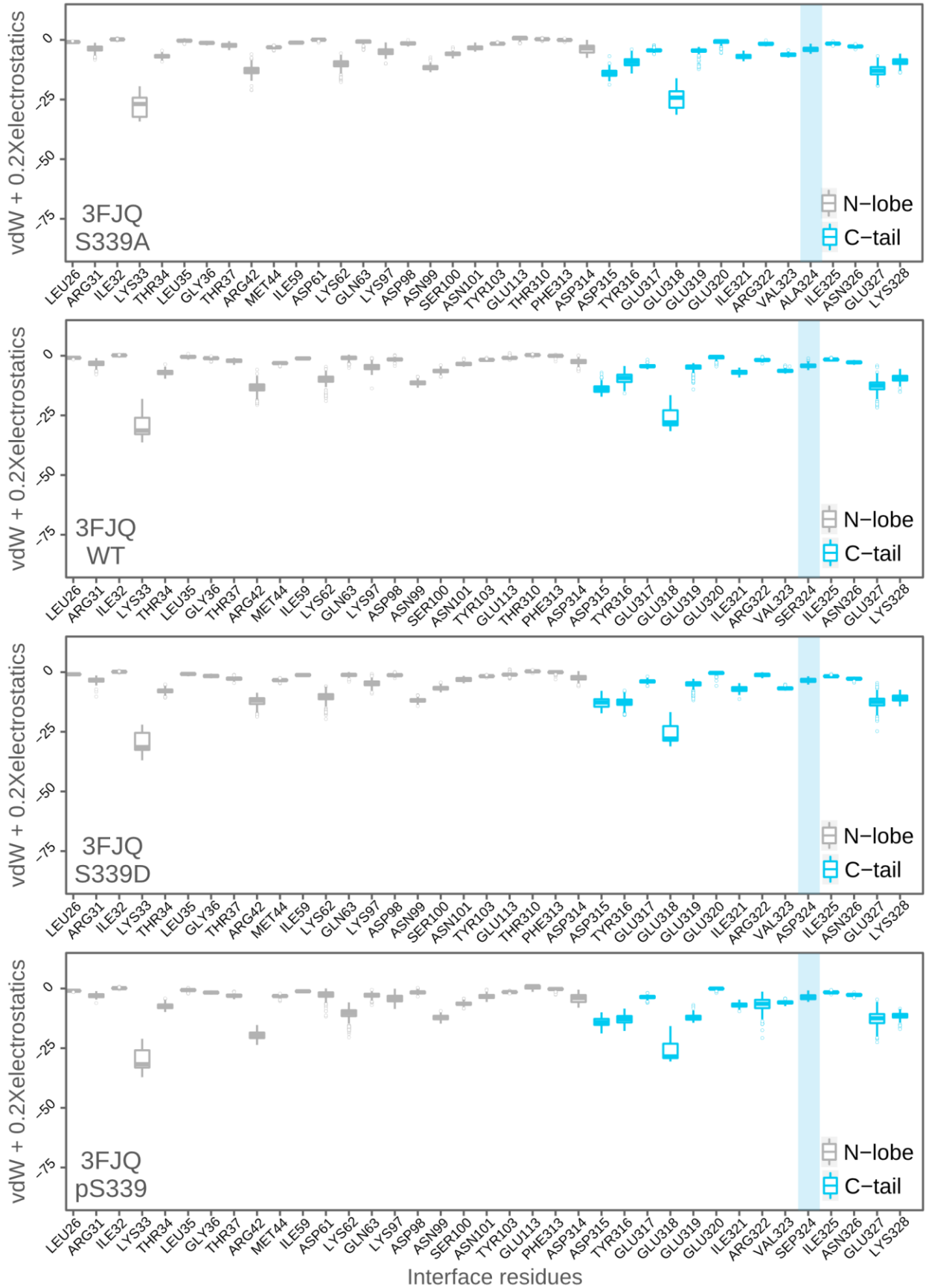


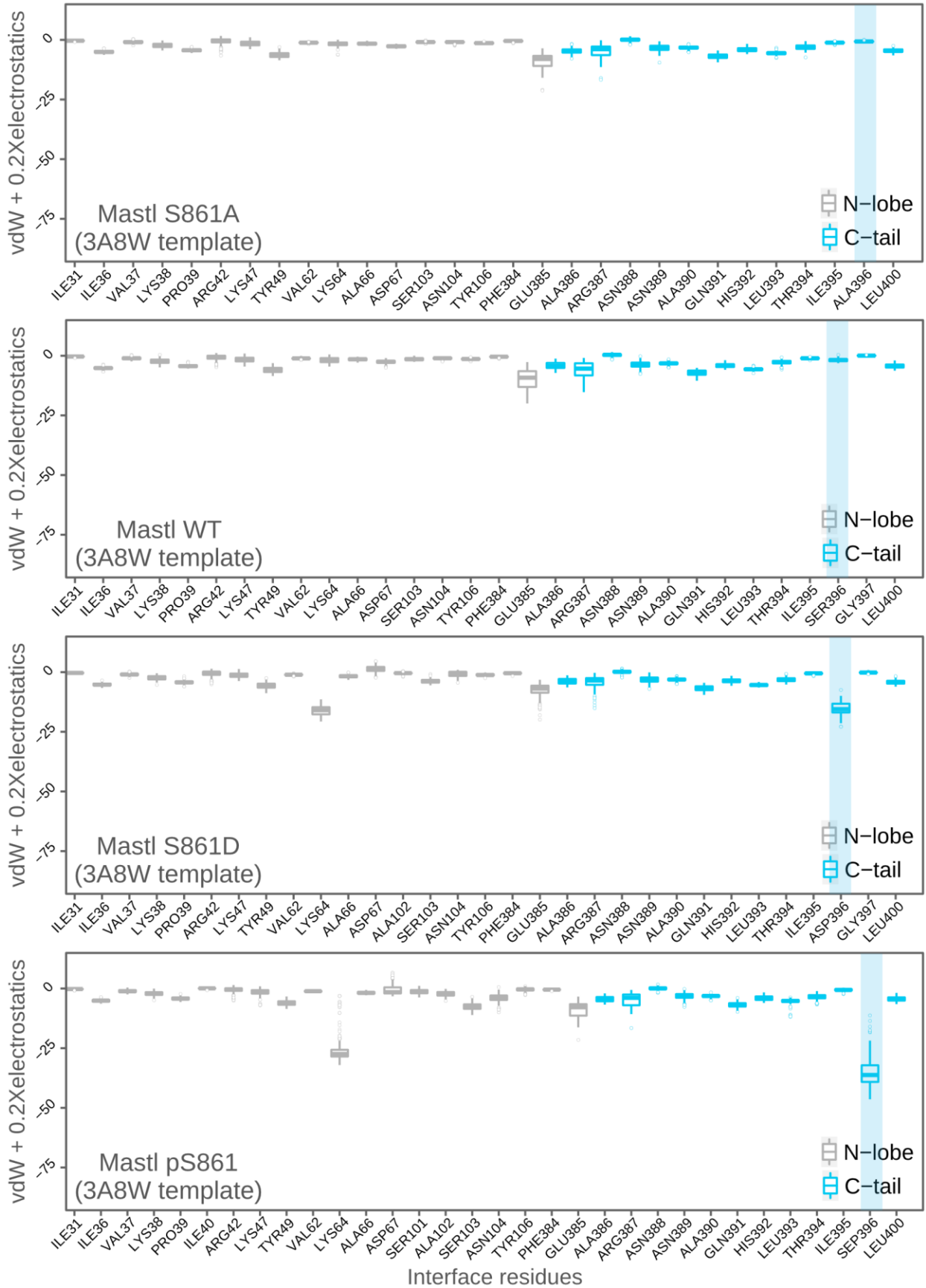


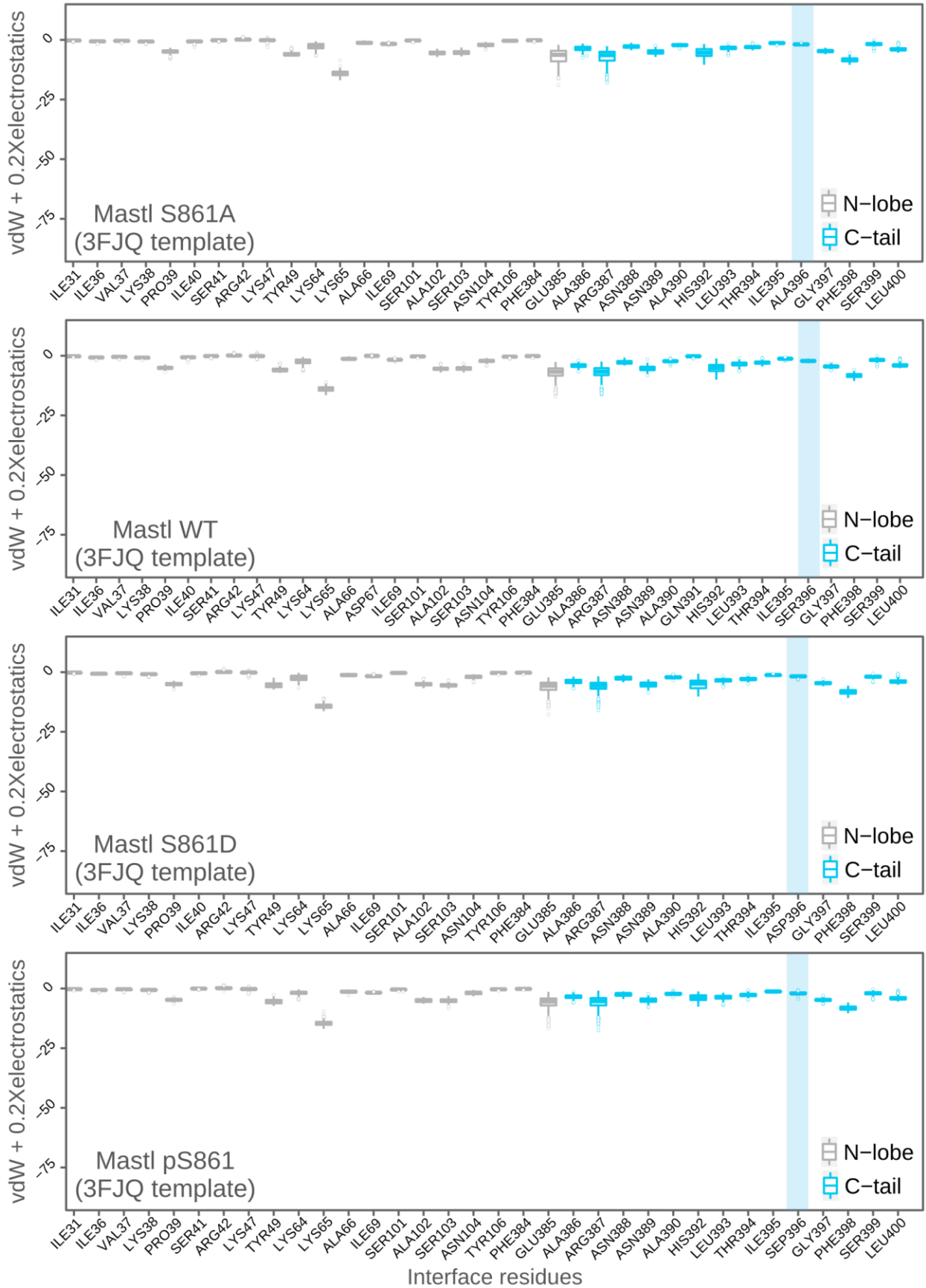


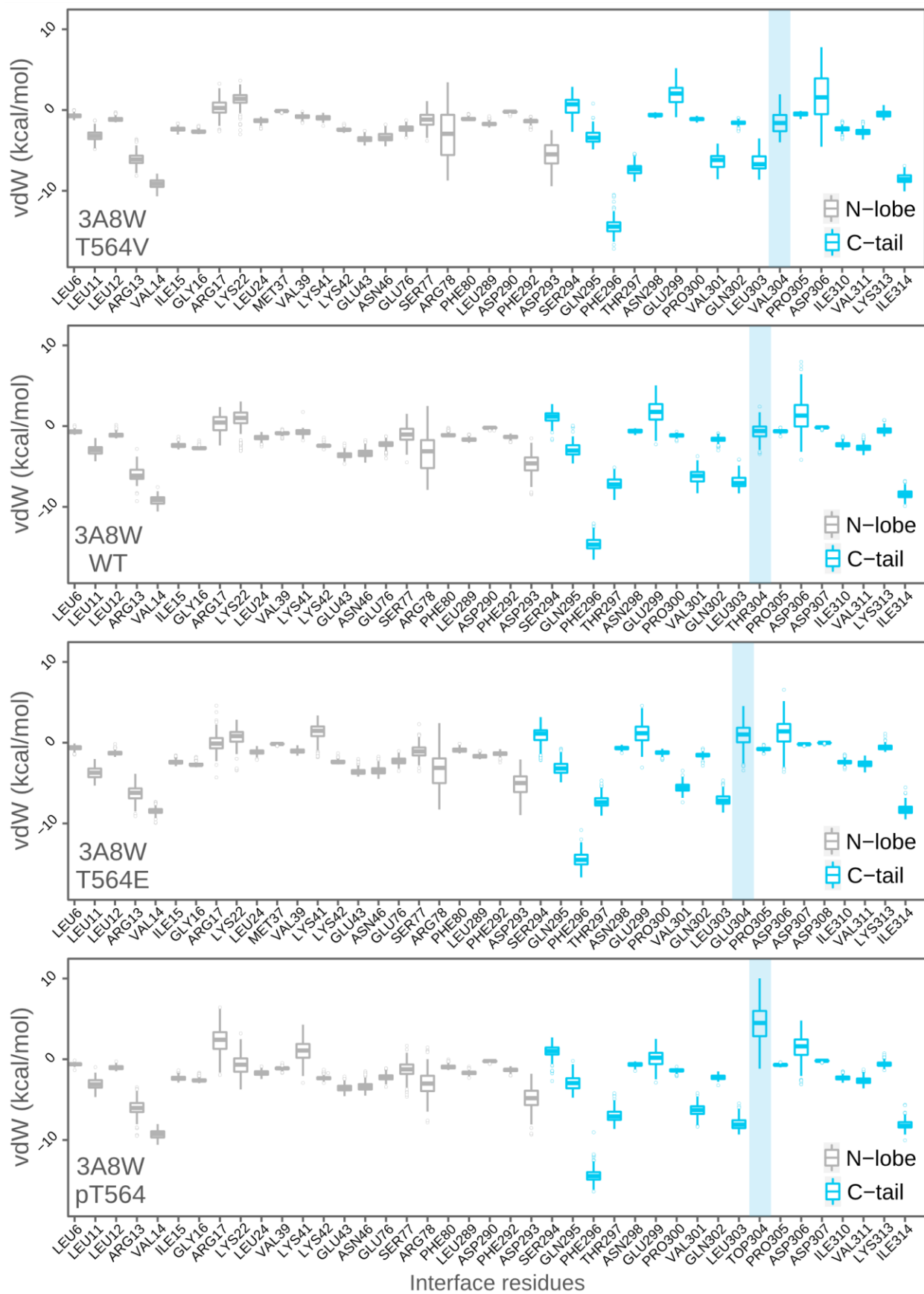


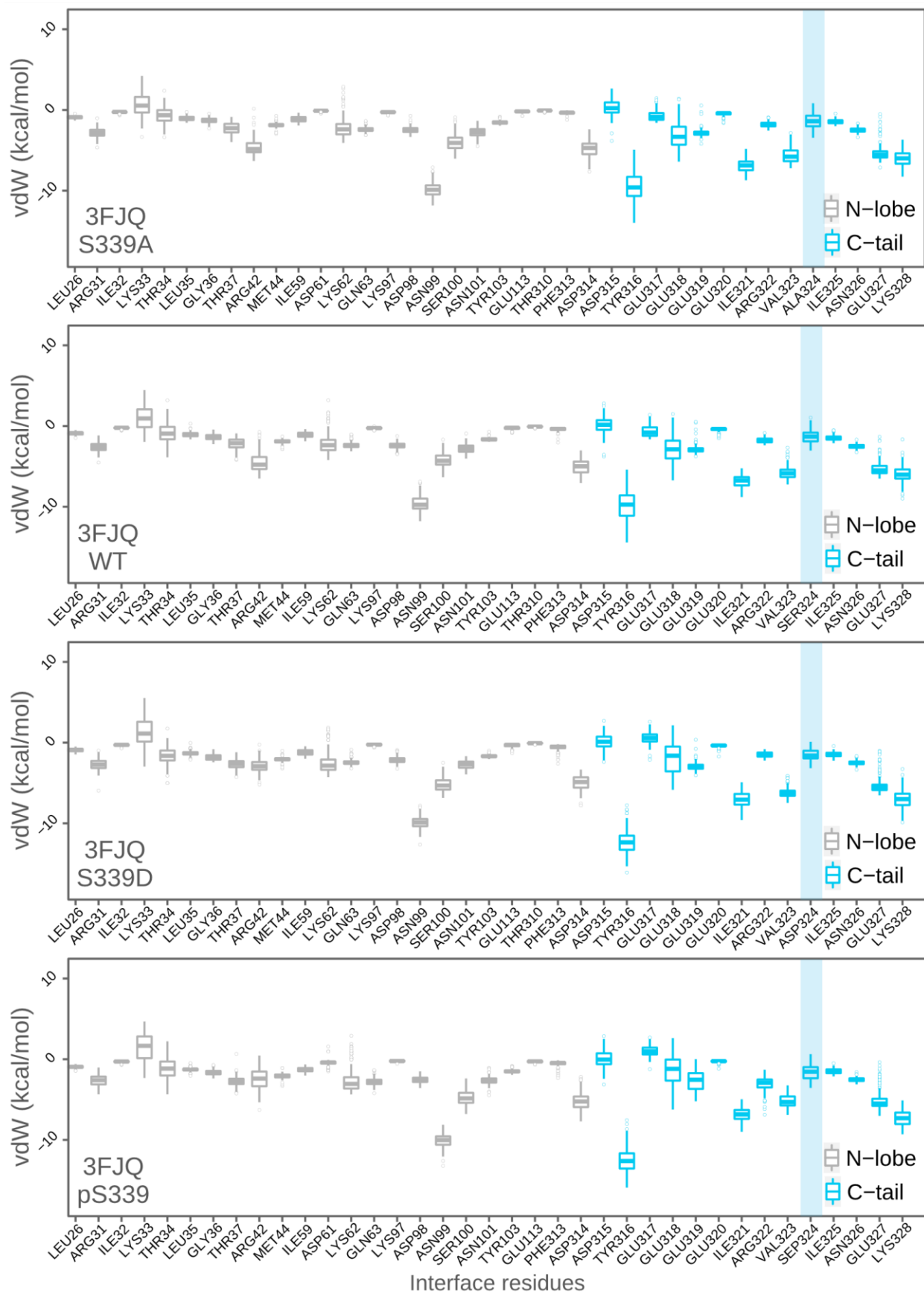


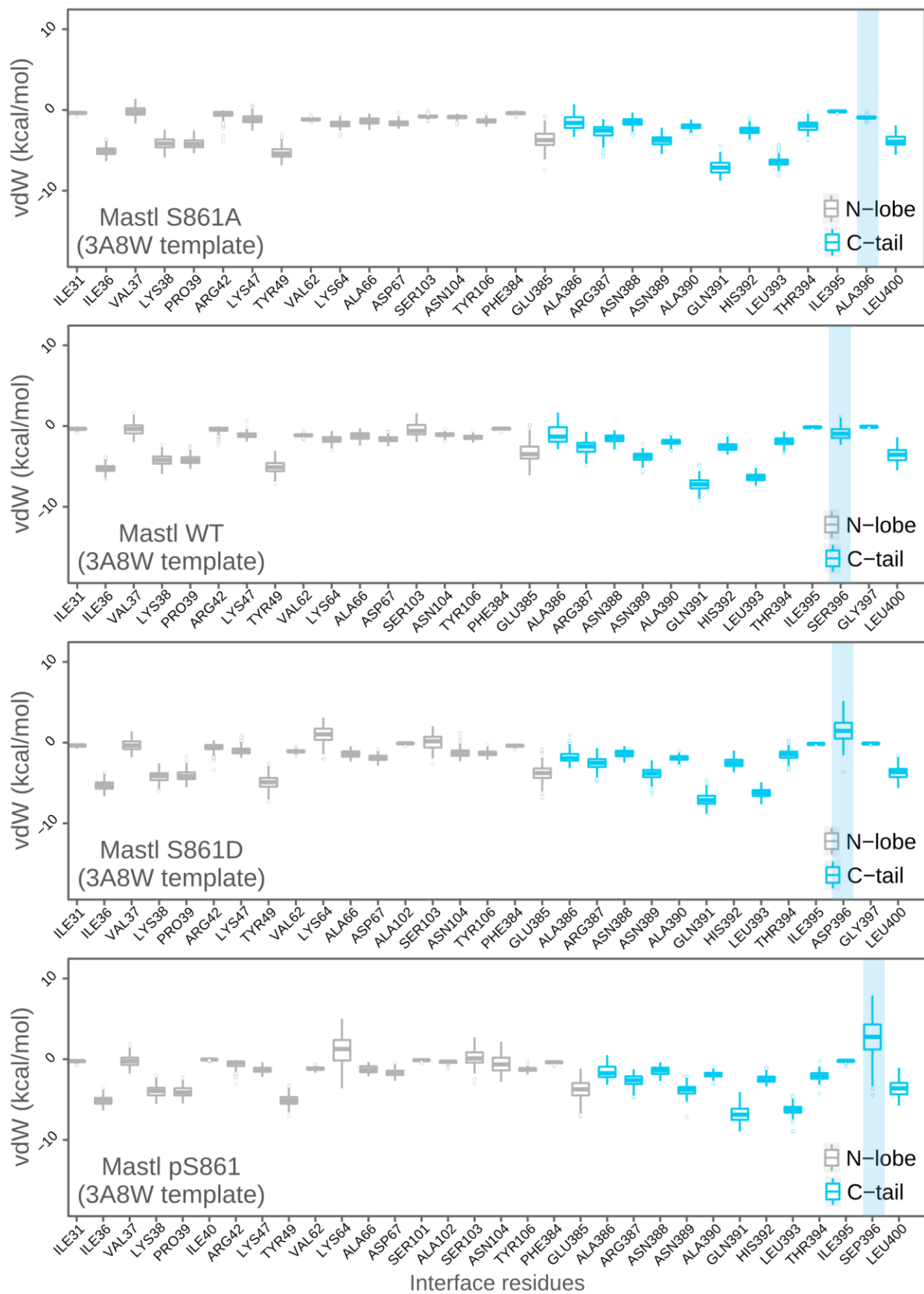












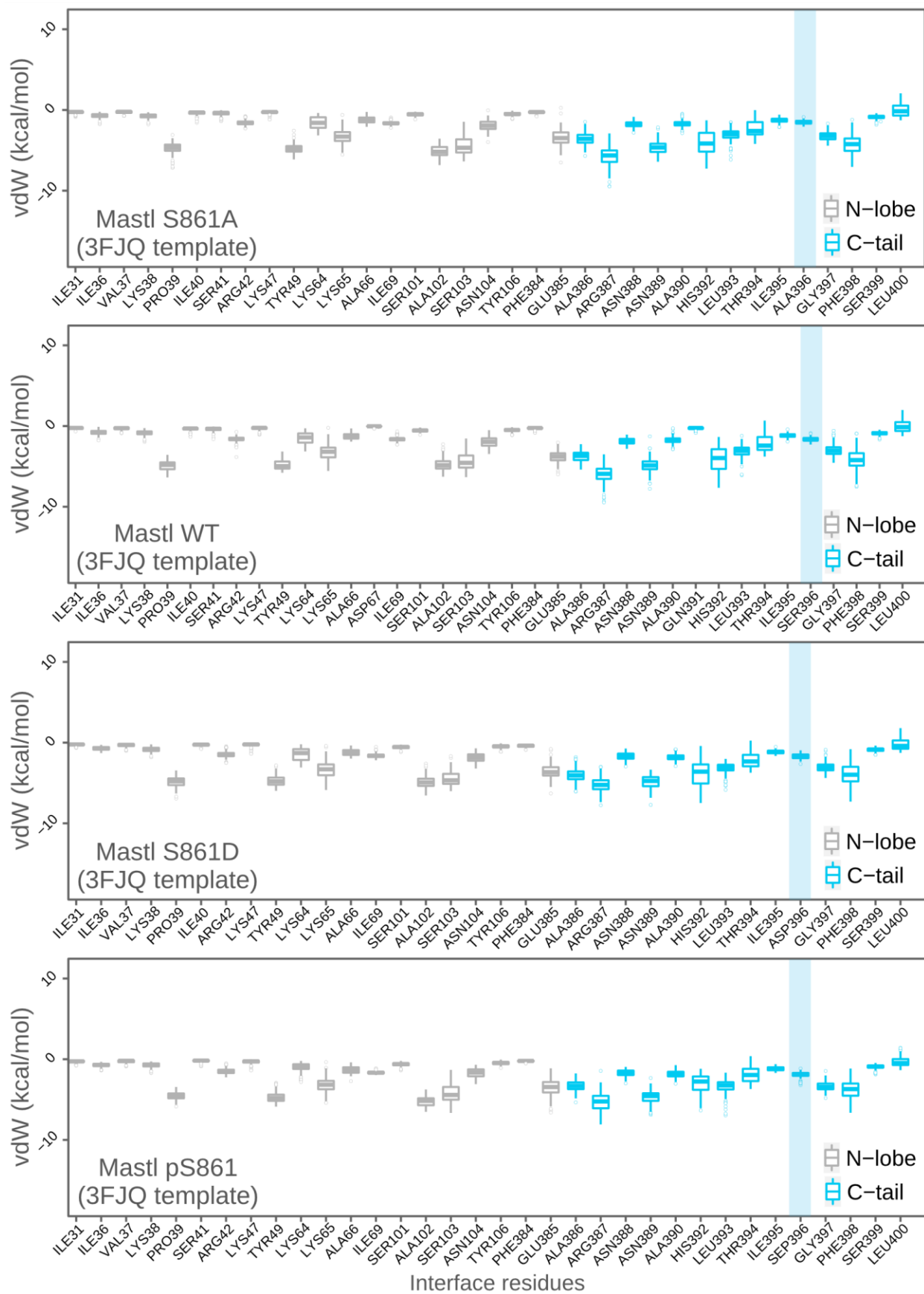


Figure S7. The PKC iota crystal structure (3A8W), PKA crystal structure (3FJQ), mouse Mastl 3A8W-based model structure, and mouse Mastl 3FJQ-based model structure were subjected to structural refinement using HADDOCK2.2 web server. For each structure, simulation results of their unphosphorylatable, wild-type, phosphomimetic, and phosphorylated forms are given. Throughout the energy minimization, HADDOCK generated 200 states for each starting structure. For each interface residue, electrostatics score, a hybrid score (vdW + 0.2 x electrostatics score), or van der Waals (vdW) scores of these 200 model structures are given as boxplots. Each box shows the energy distribution of individual interface residues throughout the simulation. The transparent blue rectangle on the right side of each plot indicates the the C-tail phosphosite. The residues are numbered according to their positions within the truncated structures. The residue number of the phosphosites within the full-length sequences are written in the bottom-left corner of each plot.

Table S1. The list of the crystal structures that contain a phosphorylated C-tail. The respective PDB entry Ids, protein names, conformation of the C-tail phosphosites, source of the enzymes, ligand content, and resolution of the structures are given. The structures used for the calculations are indicated with gray-filled rows.

PDB Id	Protein	Phosphoresidue state	Organism	Ligand	Resolution (Å)
3A8W	PKCiota	Buried	Hs	ATP	2.1
3A8X	PKCiota	Buried	Hs	-none-	2.00
1ATP	PKA	Solvent-exposed	Mm	ATP	2.2
3FJQ	PKA	Solvent-exposed	Mm	ATP	1.6
3X2U	PKA	Solvent-exposed	Mm	ATP	2.4
3X2V	PKA	Solvent-exposed	Mm	ATP	1.77
3X2W	PKA	Solvent-exposed	Mm	ATP	1.7
4DIN	PKA	Solvent-exposed	Mm	ATP	3.7
4WB5	PKA	Solvent-exposed	Hs	ATP	1.64
4WB7	PKA	Solvent-exposed	Hs	ATP	1.9
4WB8	PKA	Solvent-exposed	Hs	ATP	1.55
4XW4	PKA	Solvent-exposed	Mm	ANP	1.82
4XW5	PKA	Solvent-exposed	Mm	ATP	1.95
4XW6	PKA	Solvent-exposed	Mm	ADP	1.9
6BYR	PKA	Solvent-exposed	Hs	ATP	3.66
6BYS	PKA	Solvent-exposed	Hs	-none-	4.75
6NO7	PKA	Solvent-exposed	Hs	ATP	3.55

Table S2. Details of the primers used in this study.

Purpose	Primer ID	Primer sequence (5' to 3')	Size (bp)
PCR genotyping, FOR	KDO227	CATGCCTTCCTTGAAAGAGGTGGAC	25
PCR genotyping, REV1	KDO228	GTGGGAGGAATTACAAGAGACAAC	24
PCR genotyping, REV2	KDO198	GGCAGGTGGAGGCAAGAGCTCACAGA	26
Mouse Mastl T192V mutagenesis forward	KDO229	GGATATTCTCACAGTACCATCAATGTCTAAA CC	33
Mouse Mastl T192V mutagenesis reverse	KDO230	GGTTTAGACATTGATGGTACTGTGAGAATAT CC	33
Mouse Mastl T205V mutagenesis forward	KDO231	GATTATTCAAGAGTTCAGGACAAGTCTTAT CTCT	35
Mouse Mastl T205V mutagenesis reverse	KDO232	GTCCTGGAACCTTTGAATAATCTTGCTTAGG	31
Mouse Mastl S211A mutagenesis forward	KDO233	CAAGTCTTAGCTCTCATCAGCTCTTTGG	28
Mouse Mastl S211A mutagenesis reverse	KDO234	GCTGATGAGAGCTAAGACTTGTCTG	26
Mouse Mastl T726V mutagenesis forward	KDO235	TAGGGGTTCCAGATTACCTGGC	22
Mouse Mastl T726V mutagenesis reverse	KDO236	CAGGTAATCTGGAACCCCTAGAATTCG	27
Mouse Mastl S861A mutagenesis reverse	KDO237	CTGCAGAACCACTGTGCTGGCTACAGACTA AACCCAGCTATGGTCAGATG	50
Mouse Mastl T192E mutagenesis forward	KDO238	GGATATTCTCACAGAACCATCAATGTCTAAA CC	33
Mouse Mastl T192E mutagenesis reverse	KDO239	GGTTTAGACATTGATGGTTCTGTGAGAATAT CC	33
Mouse Mastl T205E mutagenesis forward	KDO240	GATTATTCAAGAGAACCAGGACAAGTCTTAT CTCT	35
Mouse Mastl T205E mutagenesis reverse	KDO241	GTCCTGGTTCTCTTGAATAATCTTGCTTAGG	31
Mouse Mastl S861D mutagenesis reverse	KDO242	CTGCAGAACCACTGTGCTGGCTACAGACTA AACCCATCTATGGTCAGATG	50